

1-1-2004

Computational simulation of internal blast loading on containment vessels

Kiran Kumar Matta
University of Nevada, Las Vegas

Follow this and additional works at: <https://digitalscholarship.unlv.edu/rtds>

Repository Citation

Matta, Kiran Kumar, "Computational simulation of internal blast loading on containment vessels" (2004).
UNLV Retrospective Theses & Dissertations. 1733.
<http://dx.doi.org/10.25669/8vk9-tkxz>

This Thesis is protected by copyright and/or related rights. It has been brought to you by Digital Scholarship@UNLV with permission from the rights-holder(s). You are free to use this Thesis in any way that is permitted by the copyright and related rights legislation that applies to your use. For other uses you need to obtain permission from the rights-holder(s) directly, unless additional rights are indicated by a Creative Commons license in the record and/or on the work itself.

This Thesis has been accepted for inclusion in UNLV Retrospective Theses & Dissertations by an authorized administrator of Digital Scholarship@UNLV. For more information, please contact digitalscholarship@unlv.edu.

NOTE TO USERS

This reproduction is the best copy available.

UMI[®]

COMPUTATIONAL SIMULATION OF INTERNAL BLAST LOADING ON
CONTAINMENT VESSELS

By

Kiran Kumar Matta

Bachelor of Science in Mechanical Engineering
Jawaharlal Nehru Technological University, Hyderabad, India
December 2001

A thesis submitted in partial fulfillment
of the requirements for the

Master of Science Degree in Mechanical Engineering
Department of Mechanical Engineering
Howard R. Hughes College of Engineering

Graduate College
University of Nevada, Las Vegas
December 2004

UMI Number: 1427416

INFORMATION TO USERS

The quality of this reproduction is dependent upon the quality of the copy submitted. Broken or indistinct print, colored or poor quality illustrations and photographs, print bleed-through, substandard margins, and improper alignment can adversely affect reproduction.

In the unlikely event that the author did not send a complete manuscript and there are missing pages, these will be noted. Also, if unauthorized copyright material had to be removed, a note will indicate the deletion.

UMI[®]

UMI Microform 1427416

Copyright 2005 by ProQuest Information and Learning Company.

All rights reserved. This microform edition is protected against unauthorized copying under Title 17, United States Code.

ProQuest Information and Learning Company
300 North Zeeb Road
P.O. Box 1346
Ann Arbor, MI 48106-1346



Thesis Approval
The Graduate College
University of Nevada, Las Vegas

November 02, 20⁰⁴

The Thesis prepared by

Kiran Kumar Matta

Entitled

Computational Simulation of Internal Blast Loading on Containment
Vessels

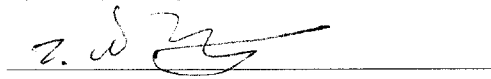
is approved in partial fulfillment of the requirements for the degree of

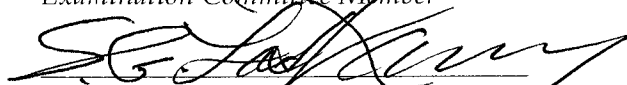
Master of Science in Mechanical Engineering


Examination Committee Chair


Dean of the Graduate College


Examination Committee Member


Examination Committee Member


Graduate College Faculty Representative

ABSTRACT

Computational Simulation of Internal Blast Loading on Containment Vessels

by

Dr. Mohamed Trabia, Examination Committee Chair
Professor and Chairperson of Mechanical Engineering
University of Nevada, Las Vegas

and

Dr. Brendan J. O'Toole, Examination Committee Chair
Associate Professor of Mechanical Engineering
University of Nevada, Las Vegas

Blast containment vessels can be an important tool for the temporary storage of explosive materials. They could be used in emergency situations for containment of explosives in public places or they could be used for planned detonations of explosive materials. The objective of this work is to verify the design procedure, and then optimize the structure for various performance levels. The near-term goal is to determine an analysis method that can accurately predict the response of a composite vessel. Various models of the containment were discussed in this report from simple to the more realistic models. Effectiveness of various models in the LSDYNA was discussed. The results from LSDYNA were compared to the results from the RFNC-VNIIEF two-dimensional results using DRAKON code and the differences between the results were discussed.

TABLE OF CONTENTS

ABSTRACT.....	iii
TABLE OF CONTENTS.....	iv
LIST OF FIGURES	vi
LIST OF TABLES.....	viii
ACKNOWLEDGEMENTS.....	viii
Chapter 1 Introduction	1
1.1 Blast Definition:.....	2
1.2 Blast Wave Profile:.....	4
1.3 Loading	6
1.3.1 Shock Pressure.....	7
1.3.2 Gas Pressure.....	8
1.4 Blast Effects	8
1.5 Blast Responses:	10
1.6 CONWEP (Conventional Weapons Effect – an Air Blast Function):.....	10
Chapter 2 Model Creation.....	12
2.1 Modeling in Solidworks and Material Properties of Parts:.....	12
2.2 Effective Material Properties Used in the Analysis:.....	14
2.3 The Properties for Each Component are Listed in the Tables 1 to 8.	22
2.4 Boundary Conditions:	27
2.5 LSDYNA Input Cards.....	28
2.5.1 Control Card.....	28
2.5.2 Database Card	29
2.5.3 Material Card	29
2.5.4 Input Cards for the CONWEP	30
Chapter 3 Modeling and discretization of various blast containment vessels	32
3.1 Model Description:	32
3.2 Modeling Details:.....	33
3.2.1 Modeling of the Container # 1	34
3.2.2 Modeling of the Container # 2	35
3.2.3 Modeling of the Container # 3	37
3.2.4 Modeling of the Container # 4.....	39

3.2.4 Modeling of the Container # 5	40
3.2.6 Modeling of the Container # 6	42
Chapter 4 Results and discussion.....	43
4.1 Results and Discussion for Container # 1	44
4.2 Results and Discussion for Container # 2	50
4.3 Results and Discussion for Container # 3	52
4.4 Results and Discussion for Container # 4	53
4.5 Results and Discussion for Containers # 5 and # 6.....	59
Chapter 5 Conclusions	67
5.1 Conclusions:.....	67
5.2 Future Goals Involved in this Project are as Follows	68
References	69
VITA.....	71

LIST OF FIGURES

Figure 1.1	Typical Pressure-Time History Plot [15]	5
Figure 2.1	Actual Drawing of the Container [1].....	13
Figure 2.2	SolidWorks Model of the Containment Vessel.....	14
Figure 2.3	Properties of the Four-Layer Laminate	16
Figure 2.4	Material Properties of Steel and Basalt	17
Figure 2.5	Final Properties of the Laminate	17
Figure 2.6	Properties of the Three-Layer Laminate.....	18
Figure 2.7	Material Properties of Basalt.....	18
Figure 2.8	Final Properties of Three Layer Laminate.....	19
Figure 2.9	Properties of the Basalt Layer with 90 Degrees	19
Figure 2.10	Final Properties of the Laminate	20
Figure 2.11	Properties of the Basalt Laminate.....	20
Figure 2.12	Final Properties of the Minus 33 Basalt Laminate	21
Figure 2.13	Properties of the 33 Basalt Laminate.....	21
Figure 2.14	Properties of the 33 Basalt Laminate.....	22
Figure 2.15	Foam Material Inside the Cap	26
Figure 2.16	Engineering Stress vs. Rectangular Foam Strain Curve.....	26
Figure 2.17	Sample Control Card.....	29
Figure 2.18	Sample Database Card.....	29
Figure 2.19	Sample Material Card.....	30
Figure 2.20	Load Segment Card for the CONWEP.....	31
Figure 2.21	Load Blast Card for the CONWEP	31
Figure 3.1	Container 1 is the Simple Solid-Shell Model	35
Figure 3.2	Container 2 with Shell and Solid Elements.....	36
Figure 3.3	Container 3 with Shell and Solid Elements.....	38
Figure 3.4	Container 3 with Gusset Plate	38
Figure 3.5	Container 4 with Shell and Solid Elements.....	39
Figure 3.6	Discretization of the Model Showing the Defects in Foam Part	40
Figure 3.7	Container 5 is Complete Solid Element Model.....	41
Figure 3.8	Meshing on the Edge of the Foam.....	41
Figure 3.9	Sixth Model of the Container	42
Figure 4.1	Container Showing the Various Locations for the Strain Plots [1]	43
Figure 4.2	Maximum Circumferential Stress at Time $t = 0.3575$ milli sec	45
Figure 4.3	Circumferential Plots for First Three Containers at # 1	45
Figure 4.4	Longitudinal Plots for First Three Containers at # 1	46
Figure 4.5	Circumferential Plots for First Three Containers at # 2	46
Figure 4.6	Longitudinal Plots for First Three Containers at # 2.....	47
Figure 4.7	Circumferential Plots for First Three Containers at # 3	47
Figure 4.8	Longitudinal Plots for First Three Containers at # 3	48

Figure 4.9	Circumferential Plots for First Three Containers at # 4	48
Figure 4.10	Longitudinal Plots for First Three Containers at # 4	49
Figure 4.11	Circumferential Plots for First Three Containers at # 5	49
Figure 4.12	Longitudinal plots Plots for First Three Containers at # 5	50
Figure 4.13	Maximum Circumferential Stress at Time $t = .14399$ milli sec	51
Figure 4.14	Maximum Circumferential Stress at Time $t = 0.1439$ milli sec	52
Figure 4.15	Maximum Circumferential Stress at Time $t = 1.8177$ milli sec	54
Figure 4.16	Circumferential Plots for the Fourth and Sixth Container at # 1	54
Figure 4.17	Longitudinal Plots for the Fourth and Sixth Container at # 1	55
Figure 4.18	Circumferential Plots for the Fourth and Sixth Container at # 2	55
Figure 4.19	Longitudinal Plots for the Fourth and Sixth Container at # 2	56
Figure 4.20	Circumferential Plots for the Fourth and Sixth Container at # 3	56
Figure 4.21	Longitudinal Plots for the Fourth and Sixth Container at # 3	57
Figure 4.22	Circumferential Plots for the Fourth and Sixth Container at # 4	57
Figure 4.23	Longitudinal Plots for the Fourth and Sixth Container at # 4	58
Figure 4.24	Circumferential Plots for the Fourth and Sixth Container at # 5	58
Figure 4.25	Longitudinal Plots for the Fourth and Sixth Container at # 5	59
Figure 4.26	Maximum Circumferential Stresses at Time $t = 3.9$ milli sec	60
Figure 4.27	Maximum Circumferential Stresses at Time $t = .79$ sec	61
Figure 4.28	Circumferential Plots for Five and Six Containers at # 1	61
Figure 4.29	Longitudinal Plots for Five and Six Containers at # 1	62
Figure 4.30	Circumferential Plots for Five and Six Containers at # 2	62
Figure 4.31	Longitudinal Plots for Five and Six Containers at # 2	63
Figure 4.32	Circumferential Plots for Five and Six Containers at # 3	63
Figure 4.33	Longitudinal Plots for Five and Six Containers at # 3	64
Figure 4.34	Circumferential Plots for Five and Six Containers at # 4	64
Figure 4.35	Longitudinal Plots for Five and Six Containers at # 4	65
Figure 4.36	Circumferential Plots for Five and Six Containers at # 5	65
Figure 4.37	Longitudinal Plots for Five and Six Containers at # 5	66

LIST OF TABLES

Table 1	Steel and Composite Shell of Cylinder.....	22
Table 2	Anti Fragment Shield and Gusset Plate	23
Table 3	Material Properties of the Throat in Cap	23
Table 4	Material Properties of the Throat in Cap	24
Table 5	Material Properties of the Outer Composite and Steel Liner for the Cap.....	24
Table 6	Given Stress –Strain Values for the Foam.....	25
Table 7	Given Stress – Rectangular Strain Values for the Foam	25
Table 8	Material Properties of the Fragment Shield.....	27
Table 9	Total Assembly (sectioned) and Cap Assembly	27
Table 10	Symmetry Boundary Conditions	28
Table 11	Details of the Blast Containment Models.....	34

ACKNOWLEDGEMENTS

I sincerely thank my thesis advisors Dr. Mohamed Trabia and Dr. Brendan J. O'Toole for their invaluable guidance and suggestions throughout the entire course of this research project.

I would like to extend my appreciation to the committee members, Dr. John Wang, Dr. Ajit K Roy, and Dr. Samaan Ladkany for their willingness to be my defense committee.

I would like to acknowledge the help of the Trevor Wilcox for his technical support.

CHAPTER 1

INTRODUCTION

Relatively light weight blast containment vessels can be an important tool for the temporary storage of explosive materials. They could be used in emergency situations for containment of explosives in public places or they could be used for planned detonations of explosive materials. Light weight vessel can be easily transported. Composite materials could be an appropriate choice for such vessel. A standardized method of analysis and design is required to ensure confidence in the performance level of a particular design. Current ASME pressure vessel codes do not account for dynamic blast loading.

Recently, Computational and experimental work performed at the Russian Federal Nuclear center (RFNC-VNIIEF) has shown the feasibility of steel-lined composite vessels for this application. The overall goal of this project is to verify the design procedure, and then optimize the structure for various performance levels. The near-term goal is to determine an analysis method that can accurately predict the response of a composite vessel. This research focuses on developing the analysis procedure of a closed cylindrical vessel with an approximate diameter of 1-m and a length of 3-m subject to an internal blast. Computational predictions for models using solid and shell elements of

strains on the outer surface of the vessel are compared to results from the report of RFNC-VNIIEF [16].

1.1 Blast Definition:

An explosion is described by a physical or a chemical change in the material with the creation of blast wave and a powerful sound. Explosion occurs under sudden change of stored potential energy into mechanical work. The explosive material can occur in two different ways. If the chemical change in the reaction zone occurs below the sonic speed through the explosive material then the explosion is considered as deflagration, where as if the chemical changes in the reaction zone occurs over the sonic speed through the explosive material in the case of a detonation. Explosion is meant as detonation unless stated otherwise in the present thesis [1].

Explosion generally produces vast destruction because of associated shock and blast waves. An explosion is a rapid release of energy in atmosphere over an extremely short time and is distinguished by the formation of shock wave subsequently resulting into a blast wave. The blast wave propagates in media and interacts with structures producing large deformations [2].

When an explosion is initiated, a very rapid exothermic chemical reaction occurs. As the reaction progresses, the solid or liquid explosive material is converted to very hot, dense high-pressure gas. The explosion products initially expand at very high velocities in an attempt to reach equilibrium with the surrounding air, causing a shock wave. A shock wave consists of highly compressed air, traveling radially outward from the source at supersonic velocities. Only one-third of the chemical energy available in most high

explosives is released in the detonation process. The remaining two-thirds is released more slowly as the detonation products mix with air and burn. This afterburning process has little effect on the initial blast wave because it occurs much slower than the original detonation. However, later stages of the blast wave can be affected by the after burning, particularly for explosions in confined spaces, as the shock wave expands pressures decrease rapidly (with the cube of the distance) because of geometric divergence and the dissipation of energy in heating the air. Pressures also decay rapidly over time (i.e., exponentially) and have a very brief span of existence, measured typically in thousands of a second, or milliseconds. An explosion can be visualized as a “bubble” of highly compressed air that expands until reaching the equilibrium with the surrounding air. [15]

Confined and contained explosions that occur within structures normally develop complicated pressure-time histories on the inside surfaces. Such loading cannot be predicted exactly, but approximations and model relationships exist to define blast loads with a good confidence. These include procedures for determination of blast loads due to initial and reflected shocks, quasi-static pressure, directional and uniform venting effects, and vent closure effects.

The shock of the blast wave is produced when the surrounding atmosphere is subject to extreme compressive pulse radiating outward from center of explosion. This wave traveling at hyper velocities represents the shock front consisting of highly compressed air at over pressures much greater than in the region behind it. This peak over pressure drops rapidly as the shock propagates outward [3]. Behind the shock the pressure of the air can drop below ambient, creating a suction effect. The shock wave traveling outwards from the source, is reflected when it meets an object with higher

density than the normal atmosphere, such as the ground. The reflected wave travels back towards the origin. The overpressure of the reflected wave may exceed the overpressure of the incident wave and due to its higher velocity will eventually catch up with the incident wave. This vertical front (known as the Mach front or Mach stem) and the incident and reflected waves meet at some distance above the ground at a point known as the triple point. The presence of limiting ground-zero distance for a Mach stem to form has been pointed out in [4].

1.2 Blast Wave Profile:

While the source and physical nature of the explosion causing the shock wave can vary greatly, the pressure-time profile of a typical blast wave can be accurately represented as in the Figure 1.1. For any arrival time T_a (where $T_a > T_d$) after the explosion (T_d), pressure at a given location jumps to a peak value of overpressure above the local ambient pressure, P_o . The pressure then decays to ambient levels in time T_d , to a partial vacuum of very small amplitude, and eventually returns to P_o . P_s is usually termed as the peak pressure. The portion of the pressure time history above initial ambient pressure is called the positive phase of the duration. The portion of the overpressure below zero is called the negative or suction phase. [7]

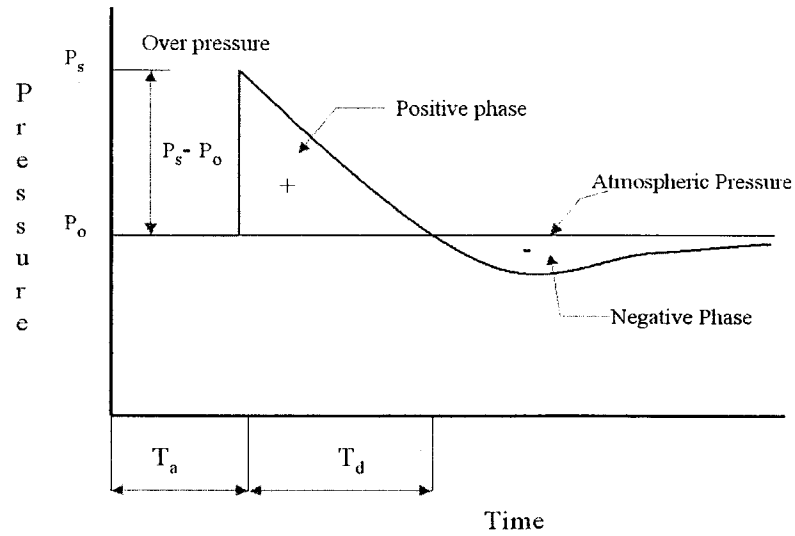


Figure 1.1 Typical Pressure-Time History Plot [15]

In order to study the effects of the blast wave on a structure, it is necessary to know the properties of the blast, such as density, wind velocity, shock front velocity, peak pressure and dynamic pressure. Blast pressures are applied as time varying blast profiles of atmospheric overpressure loading on a model. These blast profiles are the result of pressure waves that are created by the sudden and violent release of energy in the explosive charge, which causes a sharp rise in the pressure of the surrounding gas or liquid medium. In order to calculate the complete profile, the blast overpressure is needed, as well as the time of arrival and the time of duration of the positive phase and a decay coefficient. These can then be used with Friedlander's Equation to calculate the entire time history of the blast overpressure at a point [7].

$$P(T) = P_o + P_s \left(1 - \frac{T - T_a}{T_d} \right) e^{-\alpha \frac{T - T_a}{T_d}}$$

In the above equation, α is the dimensionless waveform parameter, T is the time measured from the instant the shock front arrives [6]. It has been suggested that the overpressure-time curves can be represented by triangular equivalents. These equivalent triangles have the same initial peak overpressure but have different duration depending on the expected time of maximum structural response. These durations are determined as follows:

- (a) If maximum response occurs after the overpressure has decayed to zero, duration ' T_i ' is selected so that the total impulse of the equivalent triangular curve is equal to that of the actual curve. $T_i = 2 \left[\frac{I_s}{P_s} \right]$ Where I_s is the impulse per unit of projected area obtained by integrating $P_s(t)$ from $T=0$ to $T=T_s$.
- (b) If maximum response occurs early in the pressure time history, the slope of the equivalent triangular pulse is assumed to be tangent to the actual curve, resulting in the duration T [7].

1.3 Loading

The loading from a high-explosive detonation within a confined or contained structure consists of two almost distinct phases. The first phase is the shock pressure, which typically consists of an initial high pressure, short-duration, reflected wave plus several later reflected pulses. The second is called the gas pressure in which the amplitude of the re-reflected waves usually decays with each reflection, and eventually the pressure settles to what is termed the gas pressure-loading realm [10].

1.3.1 Shock Pressure

Incident and reflected shocks inside structures consist of the initial high-pressure, short-duration reflected wave, plus several later reflected shocks, which are a result of reverberation of the initial shock within the structure. These later pulses are usually attenuated in amplitude because of an irreversible thermodynamic process. These are complicated in waveforms because of the involved reflection process within the structure, whether vented or unvented [10].

The simplest case of blast wave reflection is that of normal reflection of a plane shock wave from a plane, rigid surface. In this case, the incident wave moves at velocity U through still air at ambient conditions. The conditions immediately behind the shock front are those for the free-air shockwave. When the incident shock wave strikes the plane of surface, it is reflected and moves away from the surface with a velocity U_r into the flow field and compressed region associated with the incident wave. In the reflection process, the incident particle velocity U_s are arrested ($U_s = 0$ at the reflecting surface), and the pressure, density, and temperature of the reflected wave are all increased above the values in the incident wave.

The overpressure at the wall surface is termed as normally reflected overpressure and is designated P_r . Following the initial internal blast loading, the shock waves reflected inward will usually strengthen as they implode toward the center of the structure, and then attenuate as they move through the air and re-reflect to load the structure again. The second shocks will usually be somewhat less in strength than the initial pulse, and after several such reflections, the shock wave phase of the loading will be over [10].

1.3.2 Gas Pressure

When an explosion from a high-explosive source occurs within a structure, the blast wave reflects from the inner surfaces of the structure, implodes toward the center, and re-reflects one or more times. The amplitude of the re-reflected waves usually decays with each reflection, and eventually the pressure settles to what is termed the gas pressure-loading realm. When considering poorly vented or unvented chambers, the gas load duration can be much longer than the response time of the structure, appearing nearly static over the time to maximum response. Under this condition, the gas load is often referred to as a quasi-static load. When considering vented chambers, the gas pressure drops quickly in time as a function of room volume, vent area, mass of vent panels, and energy release of the explosion. Depending on the response time of structural elements under consideration, it may not be considered quasi-static. The gas load starts at time zero and overlaps the shock load phase without adding to the shock load, where the shock phase and the gas phase are idealized. They intersect at the load time pair (P_i , T_i) to form the bilinear load history and that should be used in design. Since the shock and gas loading are parts of the entire load history, although they are calculated separately, they should not be considered separately in design or analysis. Various procedures are available for predicting the peak gas pressure in a structure (e.g., CONWEP, Hyde 1993). The charge weight to free volume ratio has to be computed, as described in [17].

1.4 Blast Effects

Blast effects are associated with either nuclear or conventional explosive devices. Scaling laws are used to predict the properties of blast waves from large-scale explosions

based on tests on a much smaller scale [18]. The most common form of blast scaling is Hopkinson-Cranz or cube root scaling. It states that self-similar blast waves are produced at identical scaled distances when two explosive charges of similar geometry and of the same explosive, but of different sizes, are detonated in the same atmosphere. It is customary to use as a scaled distance a dimensional parameter, Z , as follows:

$$Z = \frac{R}{E^{1/3}} \text{ (or) } Z = \frac{R}{W^{1/3}} \quad (1)$$

where R is the distance from the center of the explosive source, E is the total heat of detonation of the explosive, and W is the total weight of a standard explosive such as TNT. Blast data at a distance R from the center of an explosive source of characteristic dimension d will be subjected to a blast wave with amplitude of P , duration t_d , and a characteristic time history. The integral of the pressure-time history is the impulse i . The Hopkinson-Cranz scaling law then states that such data at a distance ZR from the center of a similar explosive source of characteristic dimension Zd detonated in the same atmosphere will define a blast wave of similar form with amplitude P , duration Zt_d and impulse Zi . All characteristic times are scaled by the same factor as the length scale factor Z . In Hopkinson-Cranz scaling, pressures, temperatures, densities, and velocities are unchanged at homologous times. The Hopkinson-Cranz scaling law has been thoroughly verified by many experiments conducted over a large range of explosive charge energies. Limited reflected impulse measurements by Huffington and Ewing in 1985 showed that Hopkinson-Cranz scaling might be inapplicable for $Z < 0.4 \frac{ft}{lb^{1/3}}$ (0.16

$$\frac{kg}{m^{1/3}}) \text{ [10].}$$

The character of the blast waves from condensed high explosives is remarkably similar to those of TNT. Typical sources of compiled data for air blast waves from high explosives are for spherical TNT explosive charges detonated under standard sea level. The data are scaled according to the Hopkinson-Cranz (or cube-root) law. An acceptable set of standard air blast curves are formulated for the Positive phase blast parameters by Kingery and Bulmash (1984 Department of the Army 1986, US Departments of the Army, Navy and Air Force 1990). The procedures in [19] have been implemented in the computer code CONWEP, (Hyde 1993) which can be used for calculating a wide range of weapon and explosive effects [10].

1.5 Blast Responses:

There are two main theories to describe the blast response, the Eulerian and Lagrangian method. In Eulerian method a fixed reference in space is chosen and the motions are derived with respect to that region. The shock wave theory in this case is based on the conservation of mass, momentum and energy. In the Lagrange method, a moving reference is chosen. The stress wave theory in this case is based on the classic wave equation of motion, where equilibrium and compatibility are considered. [8]

1.6 CONWEP (Conventional Weapons Effect – an Air Blast Function):

CONWEP blast function is used to apply simple blast loading rather than to explicitly simulate the shock wave from the high explosive. The LOAD_BLAST boundary condition in LS-DYNA is based on an implementation by Randers-Pehrson and Bannister (1997) of the empirical load blast functions implemented in the CONWEP

(Conventional Weapons Effect) code (Kingery and Bulmash, 1984). The Blast functions can be used for 2 cases, the free air detonation of a spherical charge and surface detonation of a hemispherical charge. While the surface detonation approaches the conditions of a mine blast, anti-vehicular mines are most commonly buried anywhere from 5 to 20 cm (sometimes more if a road is resurfaced for example) below the surface of the soil. The depth of burial, among other things, has a significant effect on the energy directed on the target by funneling the force of the blast upwards. Other variables such as soil moisture content and soil type have an equally important effect on the mine. None of these effects are included in the CONWEP blast model and the only variable available is the mass of the explosive. [8]. CONWEP model accounts for the angle of incidence of the blast wave, but does not account for the shadowing or confinement effect. In reality when front of blast pressure hits an object, it bounds back generating secondary pressure; however, CONWEP does not however account for the secondary pressure.

1.7 Objective of the Research

The main objective of this work is to

1. Model the RFNC-VNIIEF AT 595.05 full containment vessel (RFNC AT 595.00)
2. Create various models by gradually moving toward more realistic model of the vessel. Conduct the simulations using LS-DYNA.
3. Determining the effectiveness using the material models within LS-DYNA
4. To predict the maximum deformations, failure modes in the composite or steel structure.
5. Comparing the results with the numerical simulations of [16].

CHAPTER 2

MODEL CREATION

2.1 Modeling in Solidworks and Material Properties of Parts:

A full model of the containment vessel has been shown in the Figure 2.1. AT595 container mainly consists of the cylindrical vessel with hemispherical caps on both the ends. This vessel is made of a two-layer shell with the outer layer made of basalt plastic and inner layer of stainless steel. The vessel has openings on both ends. Polymer foam has been placed to cover the end portion of the caps on either sides and is supported by damper lid to absorb the energy released by the blast. An Anti-fragment shield made of steel mesh has been placed inside the cylindrical liner to absorb the shock load. Throttles made of steel are added to increase the rigidity of the structure and attenuate the shock from the explosive materials inside the casing. The container has the inert casing for placing the explosive materials. The main parts of the vessel in the Figure 2.1 are as follows:

1. Inner Steel pressurizing layer (inner shell)
2. Outer composite bearing layer (outer shell)
3. Steel cover
4. Throat
5. Foam plastic

6. Cylindrical crusher
7. Damper lid
8. Throttling plate
9. Gusset plate
10. Cylindrical anti-fragment shield
11. Spherical anti-fragment shield
12. Hazardous item
13. Supporting- transporting arrangement.

Full containment model was created in Solid works as shown in the Figure 2.2. This model was imported to the ANSYS for meshing. The full model was extremely complex, which resulted in failure of the meshing process. It was therefore opted to use HYPERMESH as it offers more flexibility.

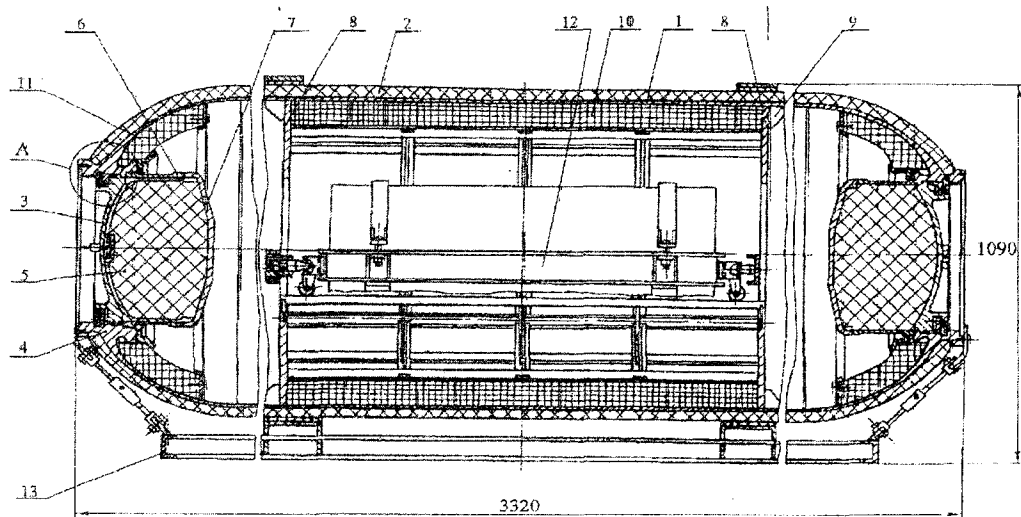


Figure 2.1 Actual Drawing of the Container [16]

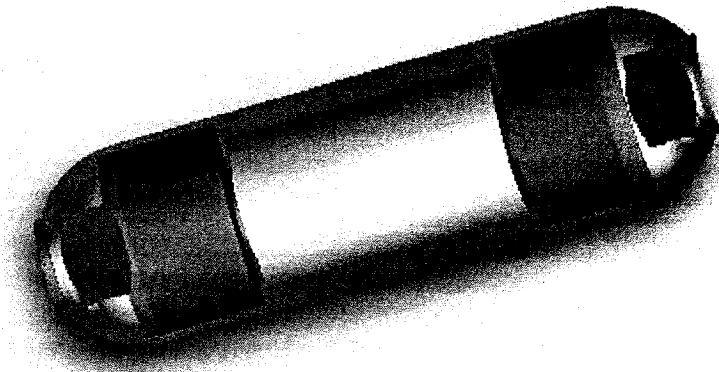


Figure 2.2 SolidWorks Model of the Containment Vessel

2.2 Effective Material Properties Used in the Analysis:

The following are the material properties of the various parts included in the blast containment vessel. Most of the Material Properties are taken from the [16]. General properties for the steel were considered as

- Density (ρ) = 8930 Kg/m³
- Poisson's ratio (ν) = .33
- Young's Modulus = 200 G Pa
- Tangent modulus = 1e5 Pa.

The outer layer of the container body is fabricated by spiral circular winding of ribbon Pb9-1200 over the inner steel shell. The ribbon consists of basalt fiber filaments with diameter of 9mm. The ribbon were impregnated with epoxy binder π T-10. Circular winding on spherical parts of container was performed in accordance with the law of geodesic profile. The angle of winding in the zones of junction between sphere and cylinder is equal to 33° and thickness of layer is 16 mm. Cylindrical part of the container has an additional layer with thickness of 16 mm with and angle of winding equals 90°.

Therefore the total thickness of basalt-plastic in central zone is 32 mm. It has a steel layer of 4.5 mm thickness inside the basalt layer.

The mechanical properties of basalt plastic layer were obtained from the final report [16] of physical and mechanical characteristics of mono directional basalt plastic. According to the experimental data from the report [16]:

- Modulus of elasticity under tension in reinforcement direction $E_1= 53.55e9Pa$
- Modulus of elasticity under tension across reinforcement direction $E_2=15.15e9Pa$
- Modulus of inter layer shear $G_{12} =5.9e9Pa$
- Poisson's ratio $\nu_{12} = .29$
- Density $\rho =2060 \frac{kg}{m^3}$

It is desirable to conduct the computational analysis using shell elements if a reasonable accuracy can be obtained. Design optimization will be easier if shell elements are used. Therefore, effective properties are estimated using classical lamination theory. Total properties of 3 layers of Basalt lamina and a single layer of Steel were estimated using the software CADEC [13]. The properties of the laminate are calculated using the CADEC software and the Figure 2.3 shows the properties of the laminate and Figure 2.4 indicates the properties of the each lamina in the laminate. The final properties of laminate used for the composite are as shown in the Figure 2.5. Similarly Figure 2.6 shows the properties of the laminate. Figure 2.7 indicates the properties of the each lamina in the laminate. The final properties of laminate used for the composite are as shown in the Figure 2.8.

Properties have also been calculated for different layers of the basalt using the CADEC and Laminator software. The values obtained from both the program's are almost the same. The following figure shows the properties calculated for the three layers of basalt and a single layer of steel using the CADEC software. Figure 2.9 is the list of the engineering properties and stacking sequence for the 90 degrees basalt lamina with thickness equal to 1.6×10^{-2} m. Figure 2.10 is the list of the final properties of the 90 degrees Basalt laminate. Figure 2.11 is the list of the engineering properties and stacking sequence for the minus 33 degrees Basalt laminate of thickness 8×10^{-2} m. Figure 2.12 is the list of the final properties of the minus 33 degree laminate. Figure 2.13 is the list of the engineering properties and stacking sequence for the 33 degrees Basalt laminate of thickness 8×10^{-2} m. Figure 2.14 is the list of the final properties for the 33-degree basalt laminate.

Filename: (1/2)

Laminate Definition for:

Number of Layers:	<input type="text" value="4"/>	Number of Materials:	<input type="text" value="2"/>	Total Thickness:	<input type="text" value="3.650E-2"/>	<input type="button" value="Plot"/>
Layer Thicknesses:	<input type="text" value=".0045 .008 .008 .016"/>					
Layup Angles:	<input type="text" value="0 33 -33 90"/>					
Layer Materials:	<input type="text" value="1 2 2 2"/>					
Loading:	Nx	<input type="text" value="0"/>	Mx	<input type="text" value="0"/>	Qx	<input type="text" value="0"/>
	Ny	<input type="text" value="0"/>	My	<input type="text" value="0"/>	Qy	<input type="text" value="0"/>
	Nxy	<input type="text" value="0"/>	Mxy	<input type="text" value="0"/>		
Temperature Change:	<input type="text" value="0"/>					
Moisture Concentration:	<input type="text" value="0"/>					
Safety Factor:	<input type="text" value="1"/>					

Figure 2.3 Properties of the Four-Layer Laminate

Number of Materials: 2

Material Number 1

E_1	200e9	E_2	200e9	G_{12}	7.692e10	G_{13}	7.692e10
G_{23}	7.692e10	ν_{12}	0.3	F_{1t}	1	F_{1c}	1
F_{2t}	1	F_{2c}	1	F_6	1	F_4	1
F_5	1	F_{12}	1	α_1	1	α_2	1
β_1	1	β_2	1	df	1		

Load Data File:

Material Number 2

E_1	53.55e9	E_2	15.15e9	G_{12}	5.9e9	G_{13}	5.9e9
G_{23}	5.9e9	ν_{12}	.29	F_{1t}	1	F_{1c}	1
F_{2t}	1	F_{2c}	1	F_6	1	F_4	1
F_5	1	F_{12}	1	α_1	1	α_2	1
β_1	1	β_2	1	df	1		

Load Data File:

Figure 2.4 Material Properties of Steel and Basalt

LaminateModuli:

Inplane		Bending	
E_x	2.425E+10	E_x^b	3.874E+10
E_y	5.092E+10	E_y^b	8.118E+10
G_{xy}	9.750E+9	G_{xy}^b	1.505E+10
ν_{xy}	0.15	ν_{xy}^b	0.142
r_N	0.000	r_M	0.022
r_B	0.000		

Figure 2.5 Final Properties of the Laminate

Filename: (1/2)

Laminate Definition for:

Number of Layers: Number of Materials: Total Thickness:

Layer Thicknesses:

Layup Angles:

Layer Materials:

Loading:

Nx	<input type="text" value="0"/>
Ny	<input type="text" value="0"/>
Nxy	<input type="text" value="0"/>

Mx	<input type="text" value="0"/>
My	<input type="text" value="0"/>
Mxy	<input type="text" value="0"/>

Qx	<input type="text" value="0"/>
Qy	<input type="text" value="0"/>

Temperature Change:

Moisture Concentration:

Safety Factor:

Figure 2.6 Properties of the Three-Layer Laminate

Number of Materials: 1

Material Number 1

Load Data File:

E_1	<input type="text" value="53.55e9"/>	E_2	<input type="text" value="15.15e9"/>	G_{12}	<input type="text" value="5.9e9"/>	G_{13}	<input type="text" value="5.9e9"/>
G_{23}	<input type="text" value="5.9e9"/>	ν_{12}	<input type="text" value="0.29"/>	F_{11}	<input type="text" value="1"/>	F_{1c}	<input type="text" value="1"/>
F_{21}	<input type="text" value="1"/>	F_{2c}	<input type="text" value="1"/>	F_{θ}	<input type="text" value="1"/>	F_4	<input type="text" value="1"/>
F_5	<input type="text" value="1"/>	F_{12}	<input type="text" value="1"/>	α_1	<input type="text" value="1"/>	α_2	<input type="text" value="1"/>
β_1	<input type="text" value="1"/>	β_2	<input type="text" value="1"/>	df	<input type="text" value="1"/>		

Figure 2.7 Material Properties of Basalt

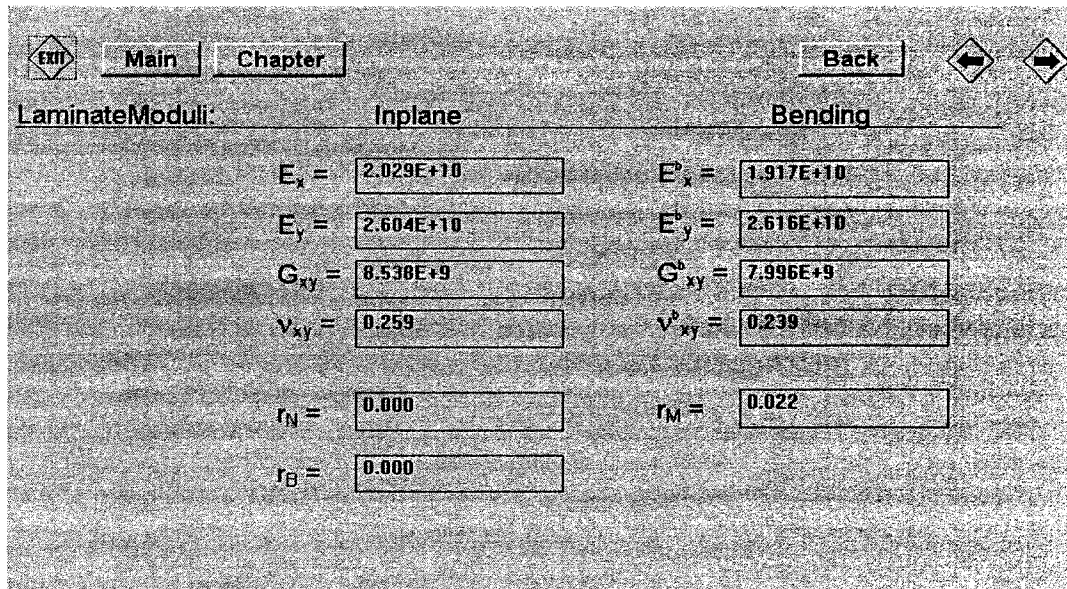


Figure 2.8 Final Properties of Three Layer Laminate

```

*****
*                               The Laminator                               *
*                               Analysis of Composite Laminates Based on    *
*                               Classical Laminated Plate Theory           *
*****

Engineering Properties
*****

Mat1      E1      E2      G12      V12
  1      5.355e+010  1.515e+010  5.900e+009  0.290

Thermal and Moisture Properties
*****

Mat1      CTE1      CTE2      CHE1      CHE2
  1      0.000e+000  0.000e+000  0.000e+000  0.000e+000

Stacking Sequence
*****

Layer      Mat1      Ply Angle      Ply Thickness
  1          1          90.0          1.600e-002
-----
Total Laminate Thickness:          1.600e-002

```

Figure 2.9 Properties of the Basalt Layer with 90 Degrees

Laminate Matrices

'ABD' Matrix

2.483e+008	7.201e+007	2.020e-008	0.000e+000	0.000e+000	0.000e+000
7.201e+007	8.777e+008	9.966e-007	0.000e+000	0.000e+000	0.000e+000
2.020e-008	9.966e-007	9.440e+007	0.000e+000	0.000e+000	0.000e+000
0.000e+000	0.000e+000	0.000e+000	5.297e+003	1.536e+003	4.309e-013
0.000e+000	0.000e+000	0.000e+000	1.536e+003	1.872e+004	2.126e-011
0.000e+000	0.000e+000	0.000e+000	4.309e-013	2.126e-011	2.014e+003

'ABD' Inverse

4.125e-009	-3.385e-010	2.691e-024	0.000e+000	0.000e+000	0.000e+000
-3.385e-010	1.167e-009	-1.225e-023	0.000e+000	0.000e+000	0.000e+000
2.691e-024	-1.225e-023	1.059e-008	0.000e+000	0.000e+000	0.000e+000
0.000e+000	0.000e+000	0.000e+000	1.934e-004	-1.587e-005	1.261e-019
0.000e+000	0.000e+000	0.000e+000	-1.587e-005	5.471e-005	-5.742e-019
0.000e+000	0.000e+000	0.000e+000	1.261e-019	-5.742e-019	4.966e-004

Apparent Laminate Engineering Properties

EX	EY	GXY	VXY	nXY, X	nX, XY
1.515e+010	5.355e+010	5.900e+009	0.082	0.000	0.000

Figure 2.10 Final Properties of the Laminate

* The Laminator *
* Analysis of Composite Laminates Based on *
* Classical Laminated Plate Theory *

Engineering Properties

Mat1	E1	E2	G12	V12
1	5.355e+010	1.515e+010	5.900e+009	0.290

Thermal and Moisture Properties

Mat1	CTE1	CTE2	CHE1	CHE2
1	0.000e+000	0.000e+000	0.000e+000	0.000e+000

Stacking Sequence

Layer	Mat1	Ply Angle	Ply Thickness
1	1	-33.0	8.000e-003
Total Laminate Thickness :			8.000e-003

Figure 2.11 Properties of the Basalt Laminate

Laminate Matrices

'ABD' Matrix

2.824e+008	9.905e+007	-9.994e+007	0.000e+000	0.000e+000	0.000e+000
9.905e+007	1.545e+008	-4.380e+007	0.000e+000	0.000e+000	0.000e+000
-9.994e+007	-4.380e+007	1.102e+008	0.000e+000	0.000e+000	0.000e+000
0.000e+000	0.000e+000	0.000e+000	1.506e+003	5.283e+002	-5.330e+002
0.000e+000	0.000e+000	0.000e+000	5.283e+002	8.237e+002	-2.336e+002
0.000e+000	0.000e+000	0.000e+000	-5.330e+002	-2.336e+002	5.880e+002

'ABD' Inverse

6.019e-009	-2.606e-009	4.421e-009	0.000e+000	0.000e+000	0.000e+000
-2.606e-009	8.425e-009	9.845e-010	0.000e+000	0.000e+000	0.000e+000
4.421e-009	9.845e-010	1.347e-008	0.000e+000	0.000e+000	0.000e+000
0.000e+000	0.000e+000	0.000e+000	1.129e-003	-4.887e-004	8.289e-004
0.000e+000	0.000e+000	0.000e+000	-4.887e-004	1.580e-003	1.846e-004
0.000e+000	0.000e+000	0.000e+000	8.289e-004	1.846e-004	2.525e-003

Apparent Laminate Engineering Properties

EX	EY	GXY	VXY	nXY,X	nX,XY
2.077e+010	1.484e+010	9.281e+009	0.433	0.734	0.328

Figure 2.12 Final Properties of the Minus 33 Basalt Laminate

```

*****
*                               The Laminator                               *
*                               Analysis of Composite Laminates Based on      *
*                               Classical Laminated Plate Theory              *
*****

Engineering Properties
*****
Mat1      E1      E2      G12      V12
1         5.355e+010  1.515e+010  5.900e+009  0.290

Thermal and Moisture Properties
*****
Mat1      CTE1      CTE2      CHE1      CHE2
1         0.000e+000  0.000e+000  0.000e+000  0.000e+000

Stacking Sequence
*****
Layer     Mat1     Ply Angle     Ply Thickness
1         1         33.0         8.000e-003
-----
Total Laminate Thickness :      8.000e-003

```

Figure 2.13 Properties of the 33 Basalt Laminate

Laminate Matrices

'ABD' Matrix

2.824e+008	9.905e+007	9.994e+007	0.000e+000	0.000e+000	0.000e+000
9.905e+007	1.545e+008	4.380e+007	0.000e+000	0.000e+000	0.000e+000
9.994e+007	4.380e+007	1.102e+008	0.000e+000	0.000e+000	0.000e+000
0.000e+000	0.000e+000	0.000e+000	1.506e+003	5.283e+002	5.330e+002
0.000e+000	0.000e+000	0.000e+000	5.283e+002	8.237e+002	2.336e+002
0.000e+000	0.000e+000	0.000e+000	5.330e+002	2.336e+002	5.880e+002

'ABD' Inverse

6.019e-009	-2.606e-009	-4.421e-009	0.000e+000	0.000e+000	0.000e+000
-2.606e-009	8.425e-009	-9.845e-010	0.000e+000	0.000e+000	0.000e+000
-4.421e-009	-9.845e-010	1.347e-008	0.000e+000	0.000e+000	0.000e+000
0.000e+000	0.000e+000	0.000e+000	1.129e-003	-4.887e-004	-8.289e-004
0.000e+000	0.000e+000	0.000e+000	-4.887e-004	1.580e-003	-1.846e-004
0.000e+000	0.000e+000	0.000e+000	-8.289e-004	-1.846e-004	2.525e-003

Apparent Laminate Engineering Properties

EX	EY	GXY	VXY	nXY,X	nX,XY
2.077e+010	1.484e+010	9.281e+009	0.433	-0.734	-0.328

Figure 2.14 Properties of the 33 Basalt Laminate

2.3 The Properties for Each Component are Listed in the Tables 1 to 8.

Table 1 shows the effective material properties of the steel and composite shell in the cylindrical portion of the vessel is as follows:

Table 1 Steel and Composite Shell of Cylinder

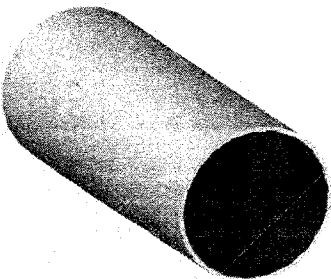
	$E_x = 24.25e9 \text{ Pa}$
	$E_y = 50.92e9 \text{ Pa}$
	$E_z = 50.92 \text{ e9 Pa}$
	$G_{xy} = 9.75 \text{ e9 Pa}$
	$\nu_{xy} = .15$

Table 2 Material Properties of Anti Fragment Shield and Gusset Plate

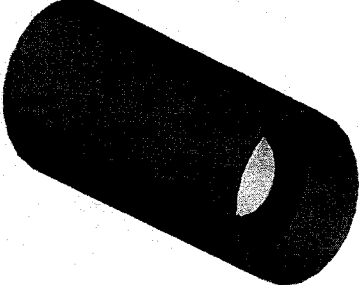
	Density = $7850 \frac{kg}{m^3}$
	Poisson's Ratio = .33
	Tangent Modulus = $1e5$ Pa
	Modulus = $500e6$ Pa

Table 3 Material Properties of the Throat in Cap

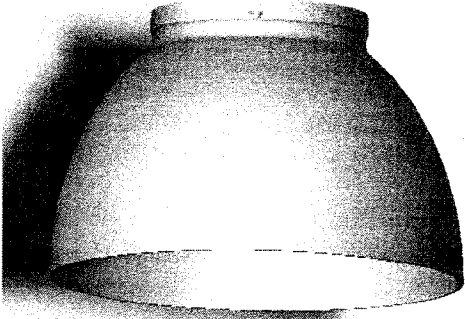
	Density = $7850 \frac{kg}{m^3}$
	Poisson's Ratio = .33
	Tangent Modulus = $1e5$ Pa
	Modulus = $500e6$ Pa

Table 4 Material Properties of the Throat in Cap

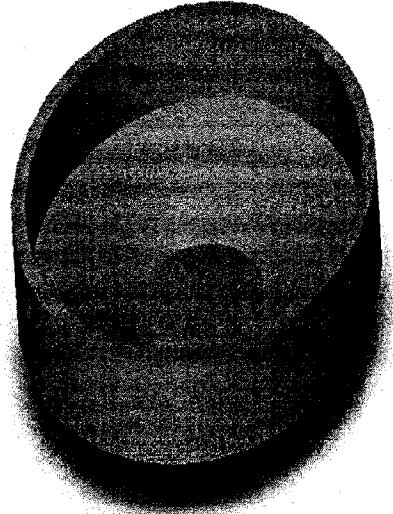
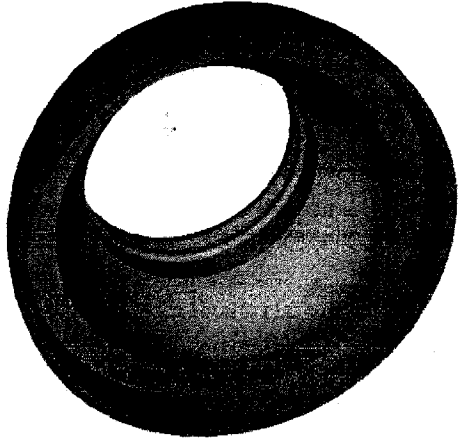
	$Density = 7850 \frac{kg}{m^3}$
	$Poisson's\ Ratio = .33$
	$Tangent\ Modulus = 1e5\ Pa$
	$Modulus = 500e6\ pa$

Table 5 Material Properties of the Outer Composite and Steel Liner for the Cap

	$E_x = 24.25e9\ Pa$
	$E_z = 50.92e9\ Pa$
	$E_y = 50.92e9\ Pa$
	$G_{xy} = 9.79e5\ Pa$
	$\nu_{xy} = .15$

The stress-strain values obtained from the report [1] are assumed to be Engineering stress-strain values. The given values for the foam are as follows:

Table 6 Given Stress –Strain Values for the Foam

Engineering Stress	Engineering Strain
0.00E+00	0
2.50E+06	0.025
3.75E+06	0.0375
5.00E+06	0.05
5.45E+06	0.1
6.36E+06	0.2
7.27E+06	0.3
7.73E+06	0.4
9.09E+06	0.5
1.00E+07	0.55
1.36E+07	0.6
3.00E+07	0.7
5.00E+07	0.73

The foam material has been assumed to be of rectangular pieces for all the calculations. Volumetric strain values have been calculated from the Engineering stress strain values using the following formula.

$$V = ((1-\nu e)^2(1+e)) - 1$$

Where V= Volumetric strain, ν = Poisson's ratio, e= Engineering strain

Table 7 Given Stress – Rectangular Strain Values for the Foam

Engineering Stress	V
0.00E+00	0
2.50E+06	-0.008707952
3.75E+06	-0.013219805
5.00E+06	-0.017838613
5.45E+06	-0.0374089
6.36E+06	-0.0820712
7.27E+06	-0.1346403
7.73E+06	-0.1957696
9.09E+06	-0.2661125
1.00E+07	-0.304943238
1.36E+07	-0.3463224
3.00E+07	-0.4370527
5.00E+07	-0.466420951

Poisson's ratio has been taken as .33 for the foam. A curve has been plotted between the Engineering stress and volumetric strain as shown in the Figure 2.16. The foam pieces have been assumed to be made of rectangular pieces. These volumetric strain values have been used in defining the curve in the MAT_CRUSHABLE_FOAM to define the behavior of the foam. Density of the foam has been given in the report [1] as $200 \frac{kg}{m^3}$ and the modulus is equal to $1.076e8$ Pa.

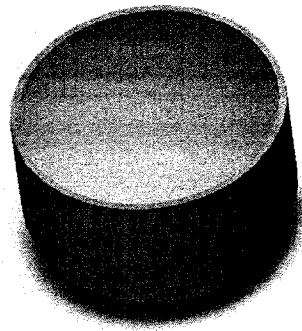


Figure 2.15 Foam Material Inside the Cap

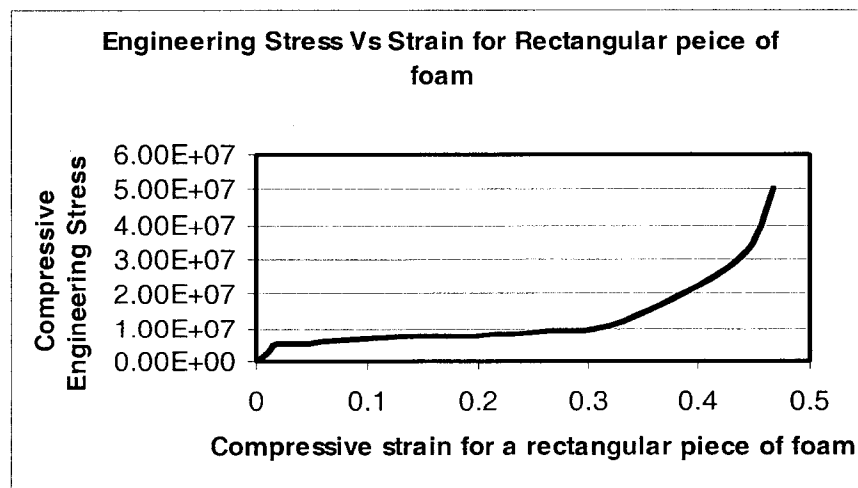


Figure 2.16 Engineering Stress vs. Rectangular Foam Strain Curve

Table 8 Material Properties of the Fragment Shield

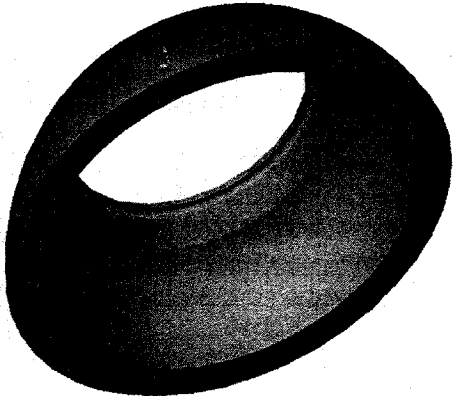
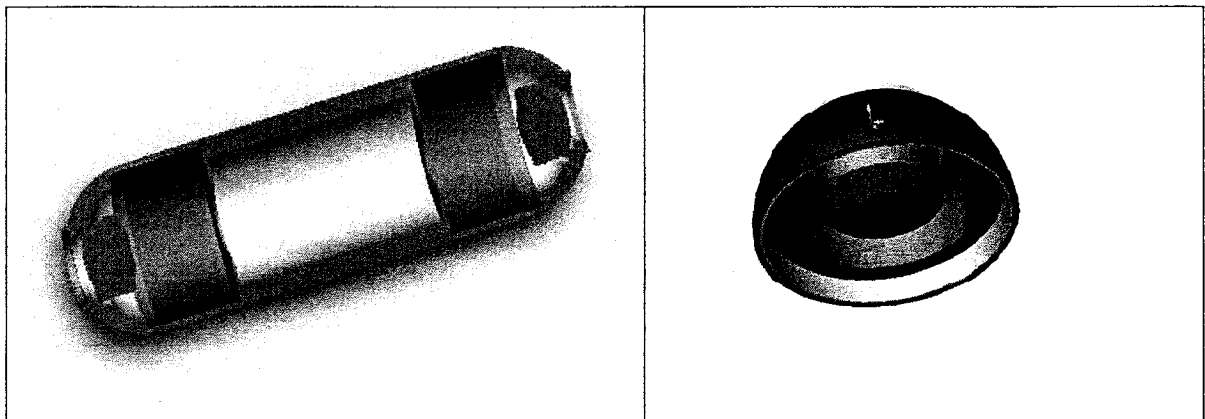
	Density = $7850 \frac{kg}{m^3}$
	Poisson's Ratio = .33
	Tangent Modulus = $1e5pa$
	Yield Stress = $800e6pa$
	$\nu_{xy} = .3$

Table 9 Total Assembly (sectioned) and Cap Assembly



2.4 Boundary Conditions:

$\frac{1}{8}$ Symmetry was used for all the containers in analysis. All the nodes in the X-

Y symmetry plane are constrained with zero rotations about the X and Y-axes and zero displacement in the Z direction. All of the translation and rotational boundary conditions

used for the $\frac{1}{8}$ symmetry model are summarized Table 10.

Table 10 Symmetry Boundary Conditions

Boundary conditions for nodes in symmetry plane	U_x	U_y	U_z	R_x	R_y	R_z
X-Y Plane			0	0	0	
Y-Z Plane	0				0	0
X-Z Plane		0		0	0	

2.5 LSDYNA Input Cards

2.5.1 Control Card

Control cards are optional cards and can be used to change the defaults, activate solution options such as mass scaling, adaptive remeshing, and an implicit solution. A control card defines the properties such as termination time, time step controls, warpage angle for shell, hourglass effect, rigid wall effect etc. A sample control card has been defined in the Figure 2.17. ENDTIME in the card defines the termination time. ENDCYC defines the termination cycle. The termination cycle is optional and will be used if the specified cycle is reached before the termination time. Cycle number identical with the time step number. DTMIN is the reduction factor for initial time step size to determine minimum time step. ENDENG is the percent change in energy ratio for termination of calculation. If undefined, this option is inactive. ENDMASS is the percent change in the total mass for termination of calculation. This option is relevant if and only if mass scaling is used to limit the minimum time step. [14]

```

*CONTROL_TERMINATION
$---+---1---+---2---+---3---+---4---+---5---+---6---+---7
$$  ENDTIM      ENDCYC      DTMIN      ENDENG      ENDMAS
      0.003      0          0.0        0.0        0.0

```

Figure 2.17 Sample Control Card

2.5.2 Database Card

Database card follows the title card. Database card defines the type of output format for results. A sample database card is shown in the Figure 2.18. DT/CYCL defines the time interval between the two outputs. LCDT is the optional load curve ID specifying the time intervals between the dumps. [14]

```

*DATABASE_BINARY_D3PLOT
$---+---1---+---2---+---3---+---4---+---5---+---6---+---7
$$  DT/CYCL      LCDT
3.0000E-05

```

Figure 2.18 Sample Database Card

Node definition follows the database card, which defines all the nodes in their respective coordinates. Section definition follows the nodes list. Section definition defines all the solid and shell sections defined in the model. Material definitions are followed by the section definition.

2.5.3 Material Card

All the material types and properties are defined in the material cards. A sample material card has been shown in the Figure 2.19. This material card was used for the Basalt-Steel composite material. MID defines the material identification. RO defines the mass density. EA defines the Young's modulus in a-direction. EB defines the Young's

modulus in b-direction. EC defines the Young's modulus in the c-direction. PRBA defines the poisson's ratio in ab. PRCA defines the poisson's ratio in ca. PRCB defines the poisson's ratio in CB. GAB defines the shear modulus in ab. GBC defines the shear modulus in bc. GCA defines the shear modulus in ca. AOPT defines material axes.

```

*MAT_ORTHOTROPIC_ELASTIC
$-----1-----2-----3-----4-----5-----6-----7-----8
$      MID      RO      EA      EB      EC      PRBA      PRCA      PRCB
      1      2773.82 .4250E+105.0920E+105.0920E+10      0.15      0.15      0.15
$-----1-----2-----3-----4-----5-----6-----7-----8
$      GAB      GBC      GCA      AOPT      G      SIGF
9.7500E+099.7500E+099.7500E+09      0.0

```

Figure 2.19 Sample Material Card

2.5.4 Input Cards for the CONWEP

Load definitions are followed by the element list. For creating the CONWEP inside the shell models three commands have been used and for solids two commands have been used. LOAD_BLAST function defines the air blast function for the application of pressure loads due to explosives in conventional weapons. This option determines the pressure values when used in conjunction with key words LOAD_SEGMENT, LOAD_SHELL and LOAD_SEGMENT_SET. LOAD_SEGMENT applies the distributed pressure load over one triangular or quadrilateral segment defined by the four nodes. The command SET_SHELL_SET generates a block of shell ID's between the starting shell ID number and an ending ID number. An arbitrary number of blocks can be specified to define the shell set. SET_SEGMENT command defines a set of quadrilateral and triangular segments with optional identical or unique attributes. [11]. A sample LOAD_SEGMENT has been shown in the Figure2.20. LCID in the LOAD_SEGMENT

card represents the load curve id. If LCID is equal to -2, then the CONWEP function is used to determine the pressure for the segments and if LCID is equal to -1, then the Brode function is used to determine the pressure for the segments. SF represents the scale factor for Load curve. AT represents the time for pressure or birth time of pressure. N1, N2, N3, N4 represents the node numbers.

```
*LOAD_SEGMENT
$-----1-----2-----3-----4-----5-----6-----7
$$      LCID      SF      AT      N1      N2      N3      N4
        -2       -1.0     0.0     696     146     144     588
```

Figure2.20 Load Segment Card for the CONWEP

A sample load blast card has been shown in the Figure2.21. The first column represents the equivalent mass of the TNT, which is equal to the eight Kg's. The next three columns represent the coordinates of x, y, z co-ordinates. TBO represents the time of explosion. IUNIT represents the unit conversion flag and the default for this column is two. The units followed are Meters, Kilograms, Seconds and Pascal's. ISURF indicates the type of blast. Default value for this column is two. In the present case two has been used here which indicates that the air blast and spherical charge of one charge diameter away from the surface.

```
*LOAD_BLAST
$-----1-----2-----3-----4-----5-----6-----7
$      WGT      XBO      YBO      ZBO      TBO      IUNIT      ISURF
        8        0        0        0        0        2        2
```

Figure 2.21 Load Blast Card for the CONWEP

CHAPTER 3

MODELING AND DISCRETIZATION OF VARIOUS BLAST CONTAINMENT VESSELS

As with modeling of any physical system, various assumptions can be used to create an equivalent mathematical model. In this section, a brief description of various models of blast containment of different solid and shell-solid cylinders is presented. CONWEP was the blast function used to apply pressure on the interior faces of the models to check the longitudinal and circumferential strains. ANSYS and HYPERMESH were used as preprocessors in the creation of the models and LSDYNA was used as the solver for all the models. LS-POST and HYPERVIEW were used as the post processors to view the results. Results were compared to the results from the reports [1]. Six models of the vessels were discussed in this chapter.

3.1 Model Description:

The description for each model is as follows:

- 1) Container # 1: This is the simplest model. Body and cap were made of shell elements. End portion of the cap is made of solid elements. This model doesn't include the interior details of the blast containment vessel.

- 2) Container # 2: Second container is similar to the first model except that the throttle plate was included using shell elements, which increases the overall rigidity of the structure. This is also a shell and solid model.
- 3) Container # 3: Third container is similar to second container except that the gusset plate was added to the throttle plate.
- 4) Container # 4: This container has accurate representation of the inner parts using the solid. All other features of this container are similar to the container #2.
- 5) Container # 5: This model is made of the brick elements completely. This model is similar to the shell container # 2.
- 6) Container # 6: This model has the gusset plates added to the throttle plate and is similar to the shell container # 3.

3.2 Modeling Details:

In all the models the outer diameter of the container was .9836 m and total length of the container is 3.25m. Thickness of .0427 m has been given to the cylindrical portion and the length of the cap end is .4 m.

Revolving the lines and areas over central neutral axes created all the models. Extruding lines and areas over the axis was the command used in the ANSYS. In ANSYS lines and curves were created using the key points and are joined to form the profiles. Profile consists of lines or areas depending on the shell or solid model respectively. Created profiles were extruded over the central neutral axis to form the three dimensional models. Meshing was done in the two dimensional stage and the meshed elements were dragged along the respective curves to create the three dimensional

models. Drag-elements over the line was the command used for HYPERMESH models. All the models were created using S.I Units. All the models have the one-eighth symmetry. Eight kilograms of TNT was exploded at the center of the vessel for all the models. CONWEP was used to create the blast inside all the cylinders. The termination time for all the models was three milli-seconds. The dimensions for all the models were represented in the table 2 as follows:

Table 11 Details of the Blast Containment Models

Outer Diameter of the vessel	.984 Meters
Length of the vessel	3.32 Meters
Thickness of the vessel in the Center portion	.036 Meters
Length of the foam	.4 Meters
Outer radius of the throttle plate	.4918 Meters
Inner radius of the throttle plate	.2292 Meters

3.2.1 Modeling of the Container # 1

First model was created using Shell and Solid elements. Cylindrical part has shell elements and end cap portion has solid elements. This model was represented in the Figure 3.1. The red portion (cylindrical portion) in the figure 3.1 has the thickness of 36.5 mm of thickness and green colored portion (cap portion) of the figure 3.1 has a thickness of 28.5 mm. Basalt–Steel composite is used for all the elements in the cylinder and cap

portion. MAT_CHRUSHABLE_FOAM is used for the foam material. True Stress Strain curve has been used in the material properties, which defines the behavior of the foam inside the cap. A mesh of 12 (circumferential) by 20 (longitudinal) was used for the body of the vessel. A mesh of 12 (circumferential) by 12 (longitudinal) was used cap and end portion of the cap that has foam in it was meshed using 8 (length) by 12 (thickness). CONWEP blast has been created inside the cylinder and the circumferential and longitudinal strains have been plotted. Total CPU run time was about 12 seconds.

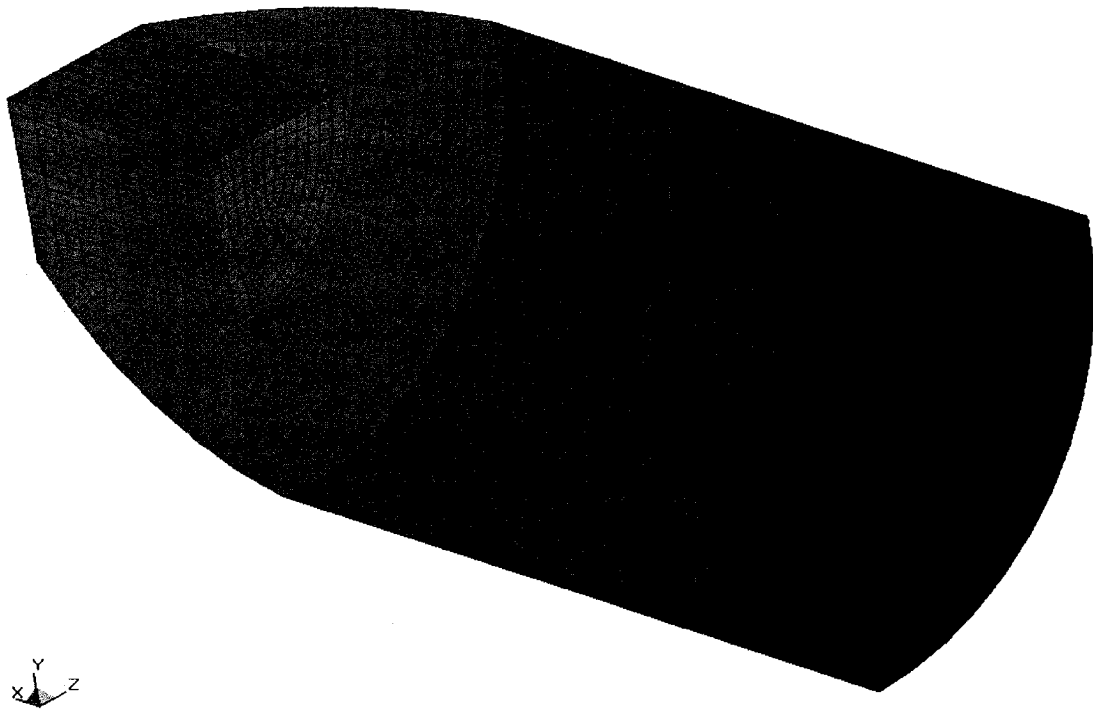


Figure 3.1 Container 1 is the Simple Solid-Shell Model

3.2.2 Modeling of the Container # 2

Second model was created using solid and shell elements. Cylindrical part and cap has Shell elements and the end portion of the cap has Solid elements. This model has been represented in the Figure3.2. The red portion (cylindrical portion) in the figure 3.1

has the thickness of 36.5 mm of thickness and green colored portion (cap portion) of the Figure 3.2 has a thickness of 28.5 mm. This model has a throttle plate added to it. The thickness of the throttle plate was 117 mm. Twelve divisions along the circumference and six divisions along the radial direction have created the meshing for the throttle. Steel was used as the material for the throttle plate. Basalt-Steel composite is used for all the elements in this cylindrical and cap portions. A mesh of 12(circumferential) by 20 (longitudinal) was used for the body of the vessel. A mesh of 12 (circumferential) by 12 (longitudinal) was used for green portion of cap and foam in it was meshed using 8 (length) by 12 (thickness). Total CPU run time was about 11 seconds.

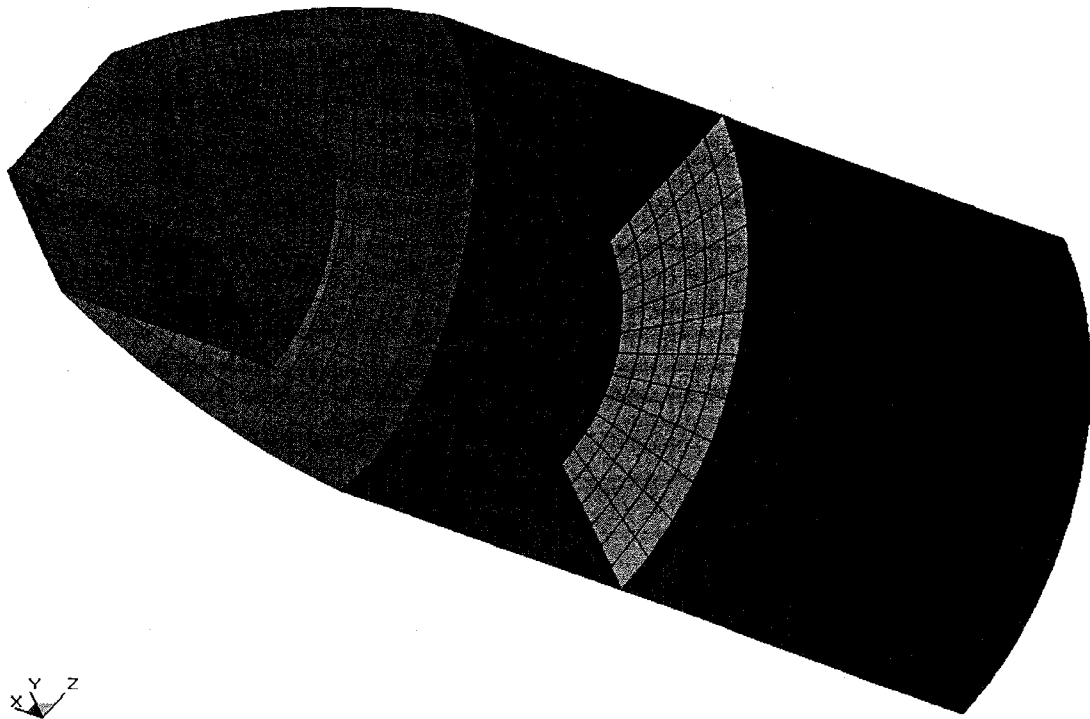


Figure 3.2 Container 2 with Shell and Solid Elements.

3.2.3 Modeling of the Container # 3

Third model was created using solid and shell elements. Cylindrical part and cap has Shell elements and the end portion of the cap has Solid elements. This model has been represented in the Figure3.3. Gusset plate added to the throttle plate was shown in the Figure 3.4. The red portion (cylindrical portion) in the figure 3.3 has the thickness of 36.5 mm of thickness and green colored portion (cap portion) of the figure 3.1 has a thickness of 28.5 mm This model has a throttle plate added to it. The thickness of the throttle plate was 117 mm. Twelve divisions along the circumference and fourteen divisions along the radial direction have created the meshing for the throttle. Gusset plate was added to the throttle plate. Twelve divisions on circumference and four divisions in the radial direction created the meshing for the gusset plate. Steel was used as the material for the throttle plate and gusset plate. Basalt-Steel composite is used for all the elements in this cylindrical and cap portions. Foam was used in the end portion of the cap. A mesh of 12(circumferential) by 20 (longitudinal) was used for the body of the vessel. A mesh of 12 (circumferential) by 12 (longitudinal) was used cap and end portion of the cap that has foam in it was meshed using 8 (length) by 12 (thickness). Total CPU run time was about 29 seconds.

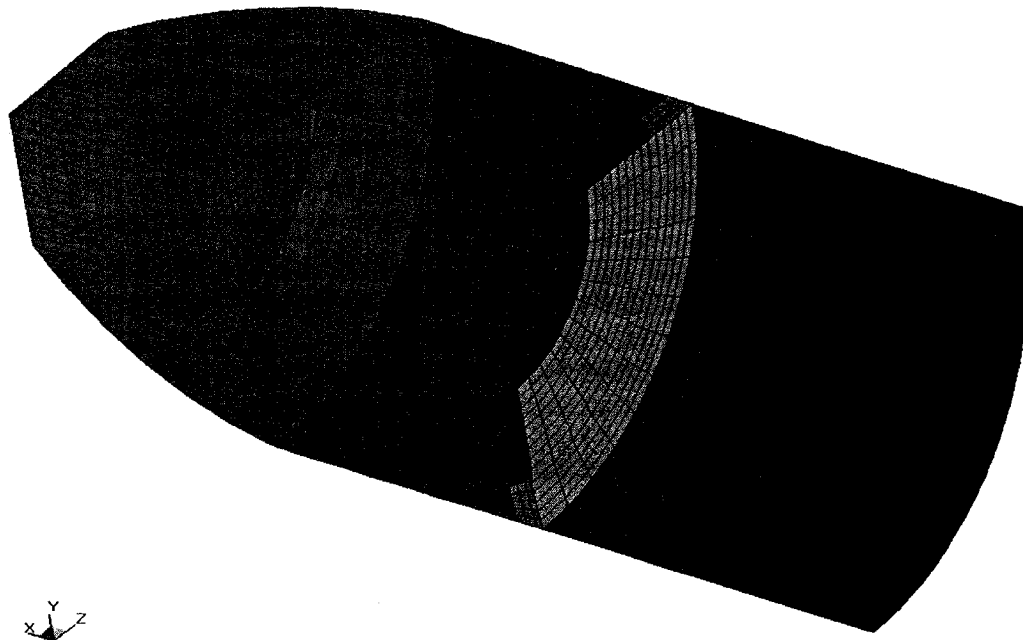


Figure 3.3 Container 3 with Shell and Solid Elements

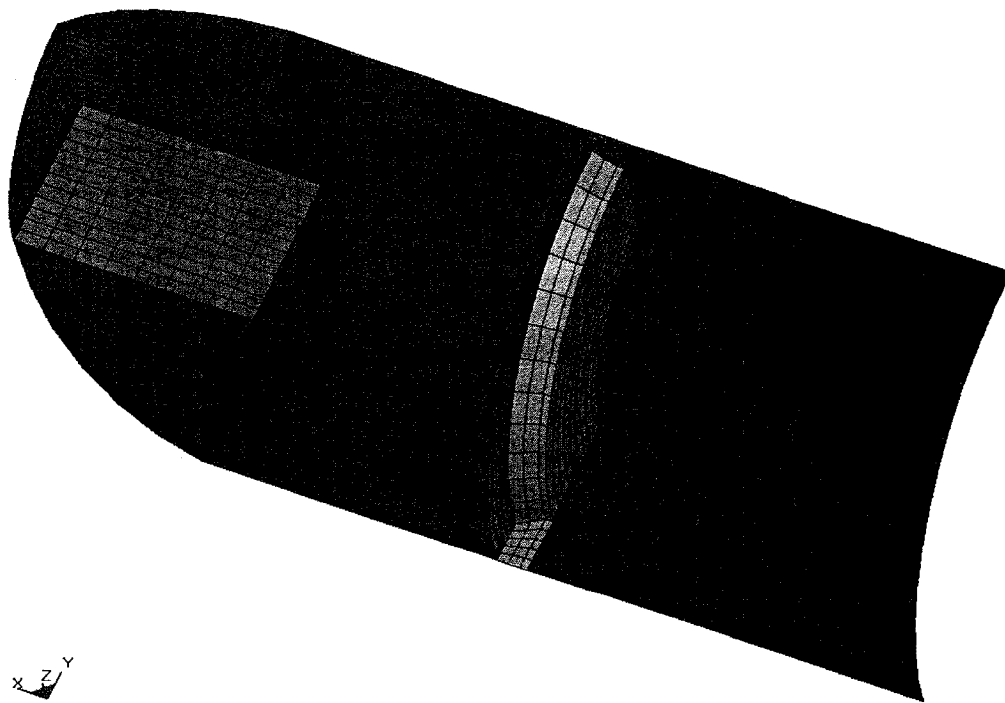


Figure 3.4 Container 3 with Gusset Plate

3.2.4 Modeling of the Container # 4

Fourth model is a more accurate representation of the AT 595 container. This model is similar to the container # 2. Most of the inner details were included. This model has been represented in the Figure3.5. This model does not include the shielding material inside the cylinder and cap. Meshing was complicated in this case. This model has refined mesh. The meshing was little complicated due to intricate parts involved in it. Cylindrical portion of the model has shell elements and cap portion has solid elements. The termination time for this model is three milli-seconds. Total CPU run time was about 7 minutes and 3 seconds. In this case there is a large variation in the aspect ratio for the elements in the cap. The meshing in the cap portion needs modification A zoomed view of the cap has been shown in the below Figure3.6.

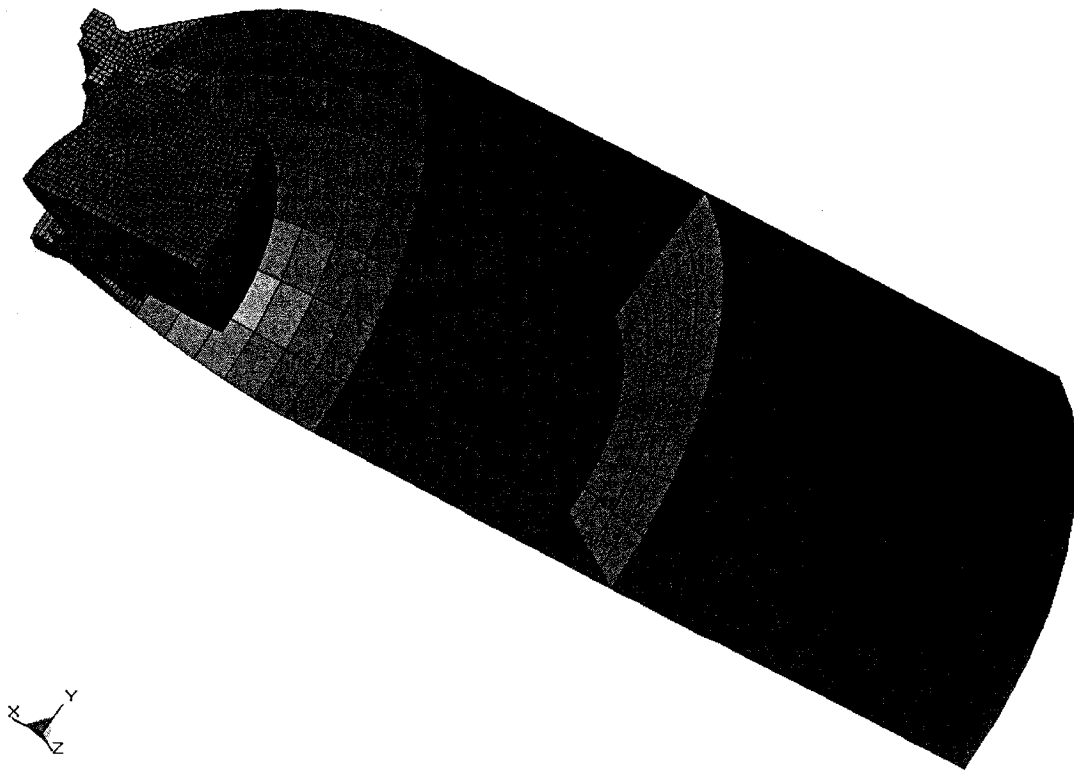


Figure 3.5 Container 4 with Shell and Solid Elements

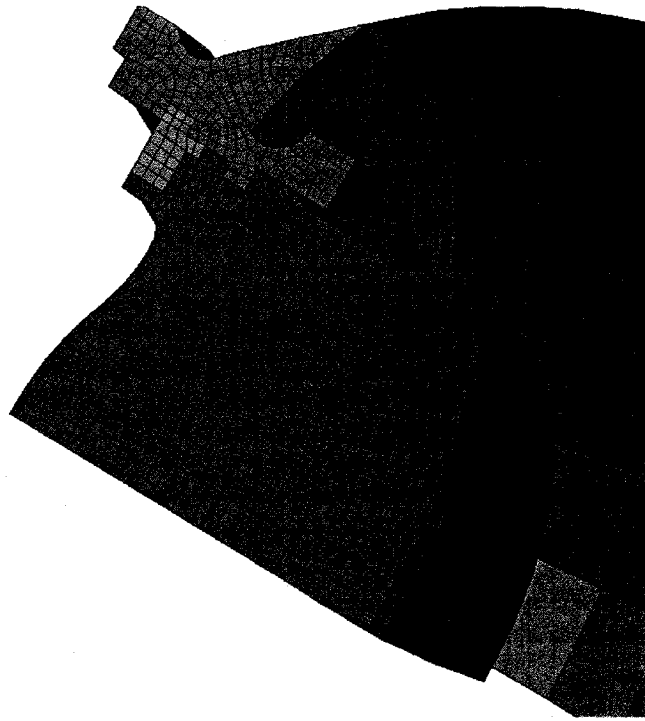


Figure 3.6 Discretization of the Model Showing the Defects in Foam Part

3.2.4 Modeling of the Container # 5

Fifth model uses only solid elements for all the parts. The meshing was denser in this case. This model has 3698811 nodes and 280390 elements. This is a complete solid model. Fifth model has been represented in Figure 3.7. This model is similar to the second model, which has shell in the cylindrical part. It has four layers of materials in the cylindrical part. Top three layers were calculated equivalent properties of composite layers and the bottom layer has steel properties. The CONWEP blast is applied at the center of the cylinder using the load_blast command. Mesh in this foam has been rectified. Total CPU run time was about four hours forty-three minutes and twenty-one seconds with three CPU parallel processing on cluster.

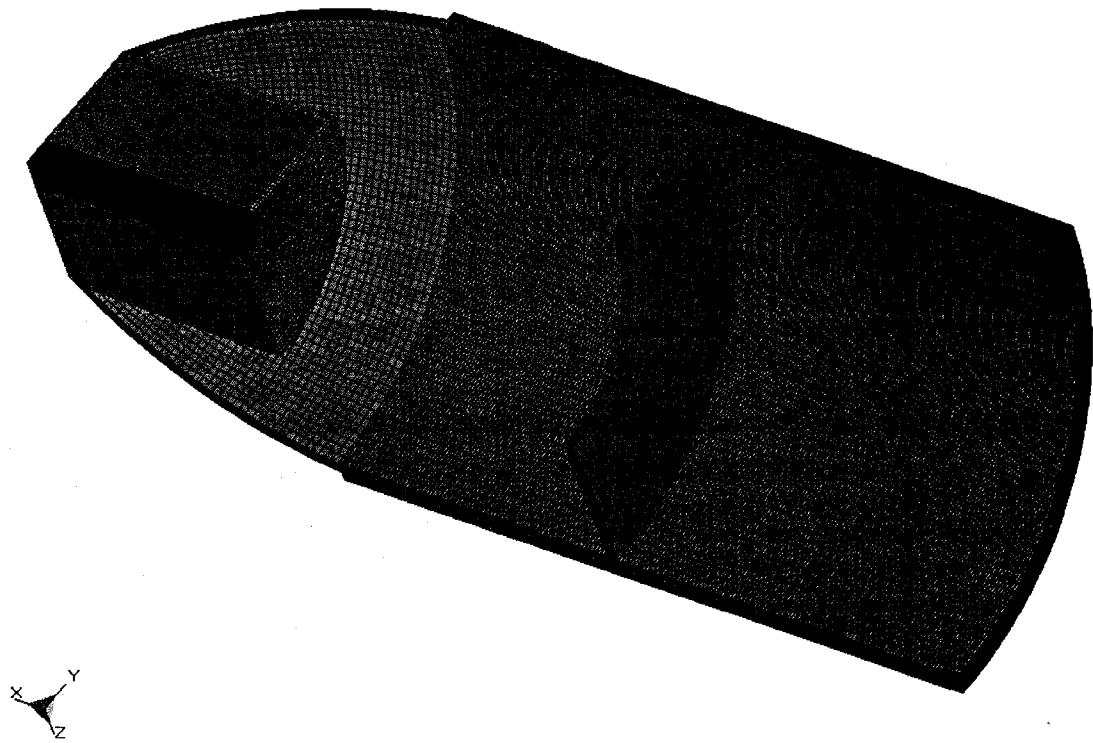


Figure 3.7 Container 5 is Complete Solid Element Model

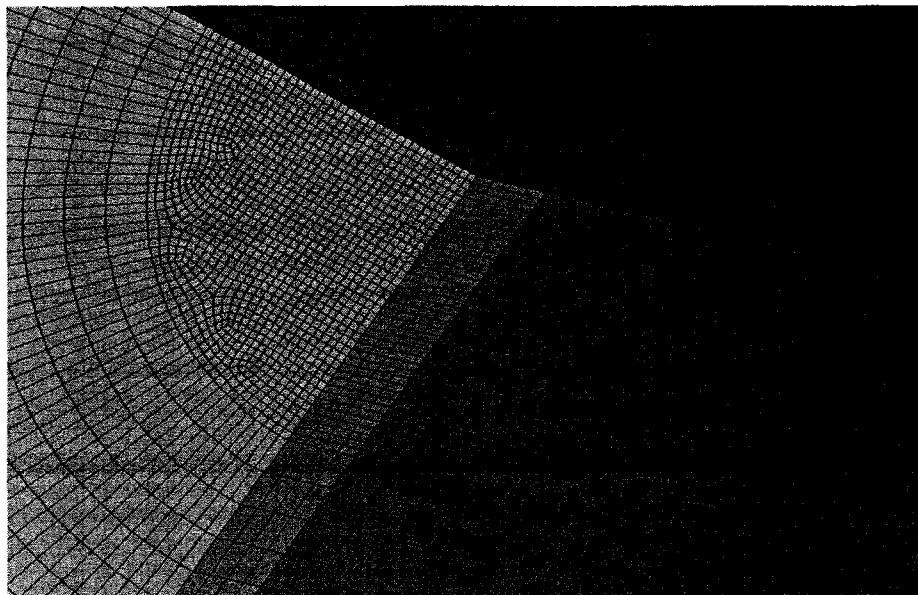


Figure 3.8 Meshing on the Edge of the Foam

3.2.6 Modeling of the Container # 6

Sixth model uses only solid elements for both the cylindrical part and all other parts. The meshing was denser in this case. This model has five-gusset plates on the throttle plate. This model has 329287 elements and 372381 nodes. This model is similar to the fourth model but it has gusset plate added to the throttle plate. It has four layers of materials in the cylindrical part. Top three layers were calculated equivalent properties of composite layers and the bottom layer has steel properties. The CONWEP blast is applied at the center of the cylinder using the load_blast command. Mesh in this foam has been rectified. Total CPU run time was about twelve hours thirty-two minutes and twenty seconds. Sixth model was represented in the Figure 3.9.

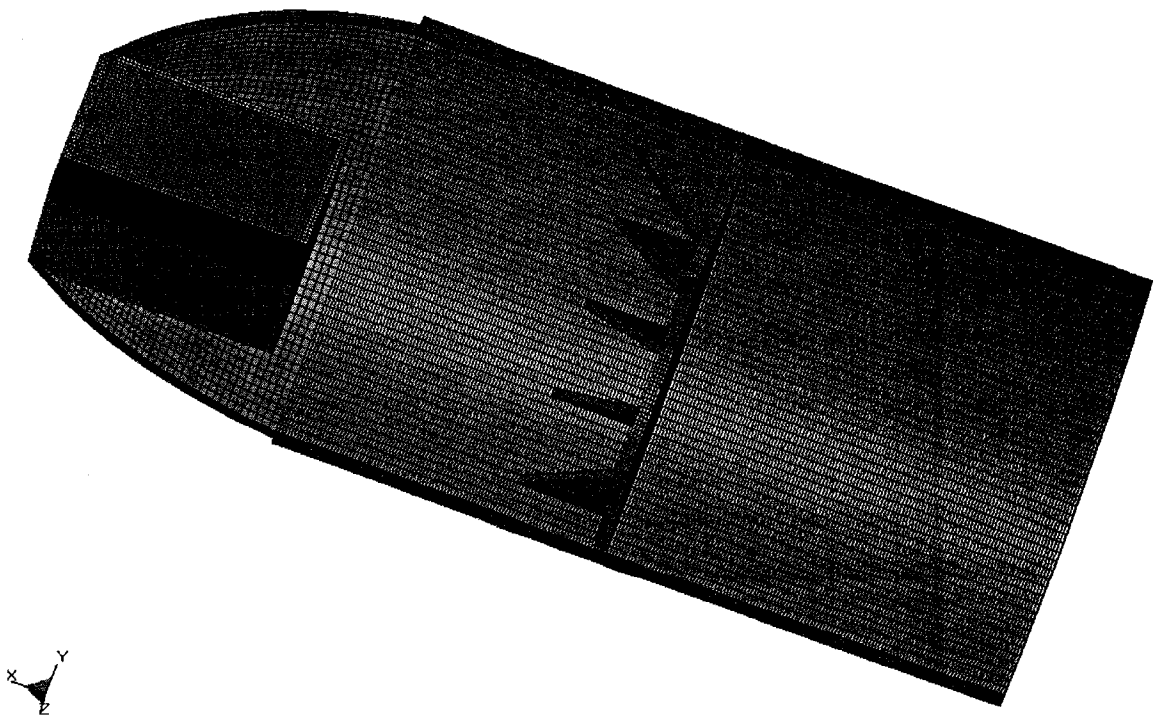


Figure 3.9 Sixth Model of the Container

CHAPTER 4

RESULTS AND DISCUSSION

Results for the previous models described in the previous chapter have been compared to the Russian reports [1]. The results in the Russian reports used for comparison are the results of the computational simulations of the DRAKON code for the two dimensional models. In these results longitudinal and circumferential strains are compared to that of the report. These results from the reports were compared to the results from the LS DYNA. Strain plots were plotted for all the models at five different points for each cylinder as shown in the Figure 4.1

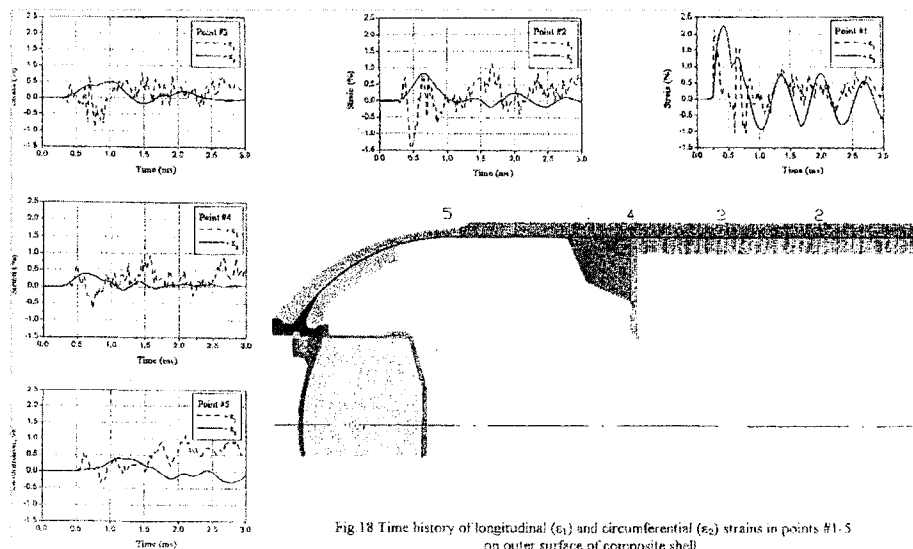


Figure 4.1 Container Showing the Various Locations for the Strain Plots [1]

4.1 Results and Discussion for Container # 1

The results for the first vessel model are as follows. Deformed Shapes, displacements and stresses were generated using LS-Post and Hyper-view. The following Figure 4.2 represents the maximum circumferential stress as 879.8 mega pascal's at time equal to .36 milli seconds. The strain histories for the first three models were compared to the results from the reports [1]. From the Figure 4.3, it is observed that the circumferential strains are less in magnitude and the material seems to be more elastic when compared to the results form the report [1]. Reduction in the magnitude may be due to the replacement of different materials with a single shell. A phase shift in the circumferential plots was observed. From the following longitudinal strain plot Figure 4.4 it is observed that the strain in the longitudinal direction is smaller in magnitude when compared to the results from the report [1]. The chosen shell element is unable to capture the peak strains in the longitudinal direction. The frequency of peaks and valleys are more in case of the results from the reports [1]. The peak circumferential strain value at the point 2 is greater in magnitude than the peak value from the report [1], which is due to the more elastic nature of the shell element. The peak strain at this point is less than the previous point. The circumferential plots at the points 3 and 4 are reduced in magnitude when compared to the previous points but due to the elastic nature of the element the strains were more incase of the observed results from LSDYNA. The circumferential plot at point 5 was quite different from the other plots and the reason may be due to the sudden reduction in the thickness. The reduction in the longitudinal strains at other points may be due to the material, which is unable to capture the strains in the longitudinal direction.

CYLINDER BLASTING MODEL
 Time = 0.00035752
 Contours of Effective Stress (v-m)
 max ipt. value
 min=-1.01068e-021, at elem# 847
 max=8.79809e+008, at elem# 301

Fringe Levels
 8.798e+008
 7.918e+008
 7.038e+008
 6.159e+008
 5.279e+008
 4.399e+008
 3.519e+008
 2.639e+008
 1.760e+008
 8.798e+007
 1.011e-021

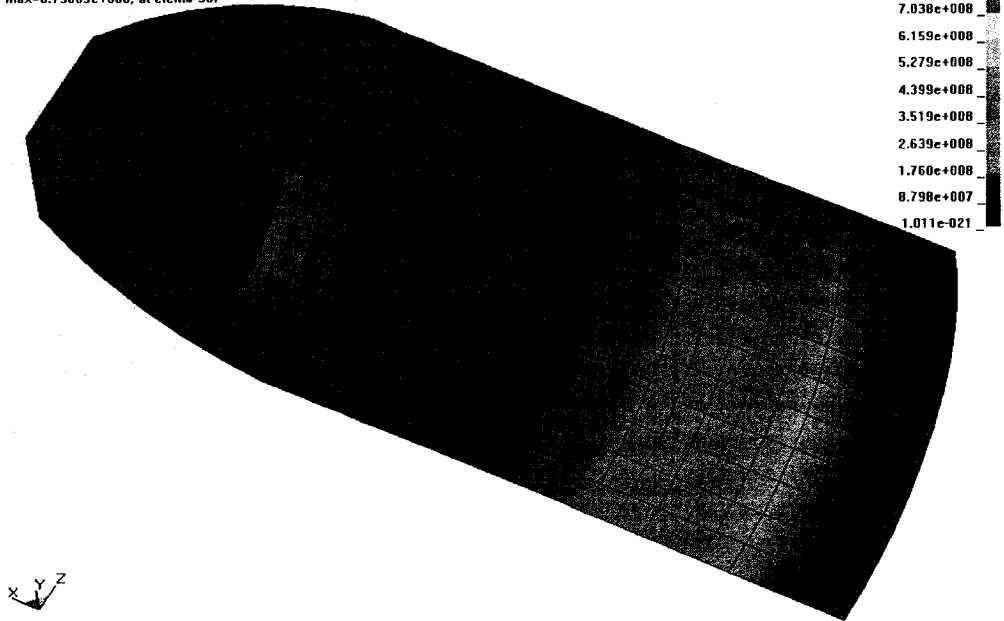


Figure 4.2 Maximum Circumferential Stress at Time $t = 0.3575$ milli sec

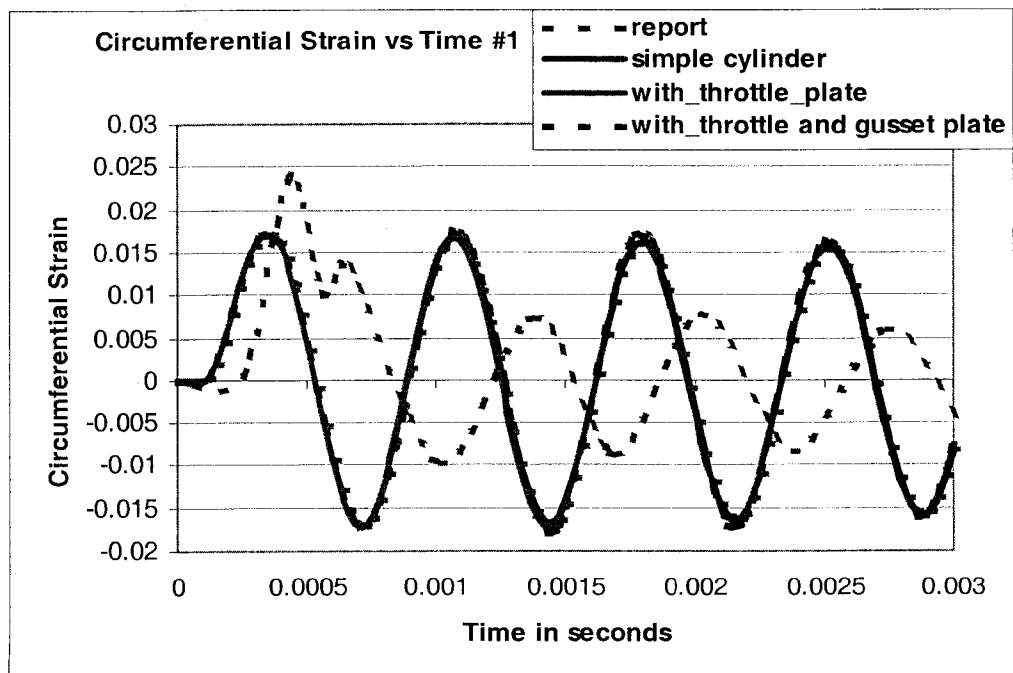


Figure 4.3 Circumferential Plots for First Three Containers at # 1

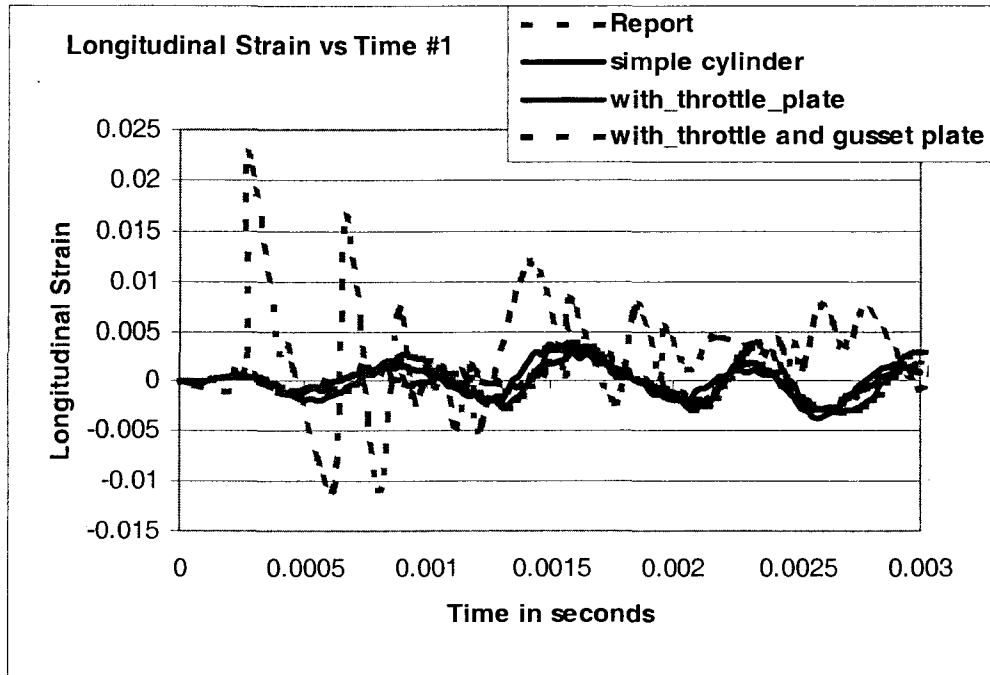


Figure 4.4 Longitudinal Plots for First Three Containers at # 1

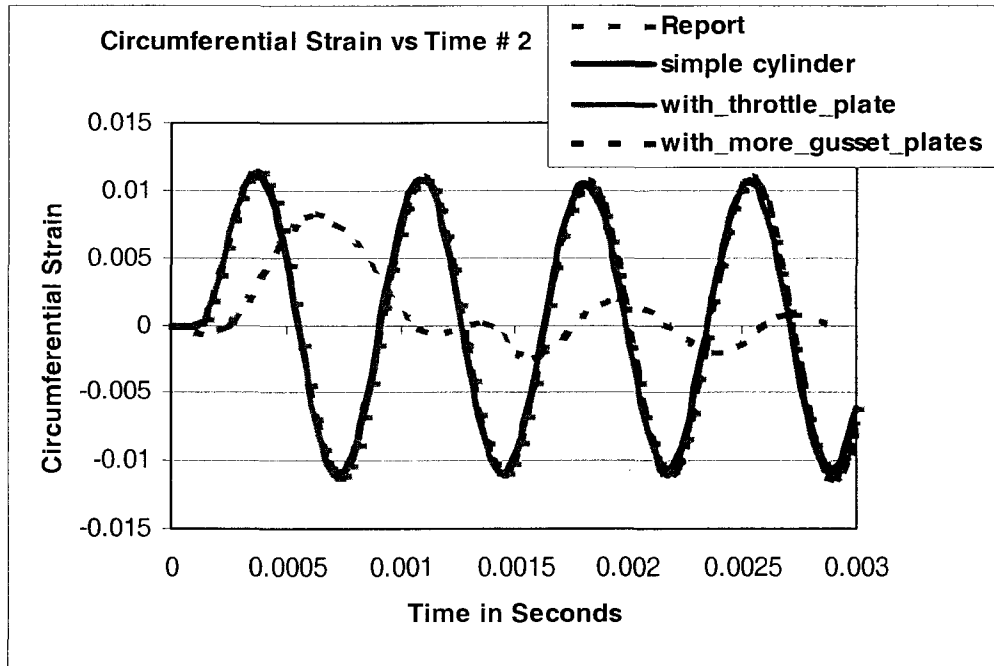


Figure 4.5 Circumferential Plots for First Three Containers at # 2

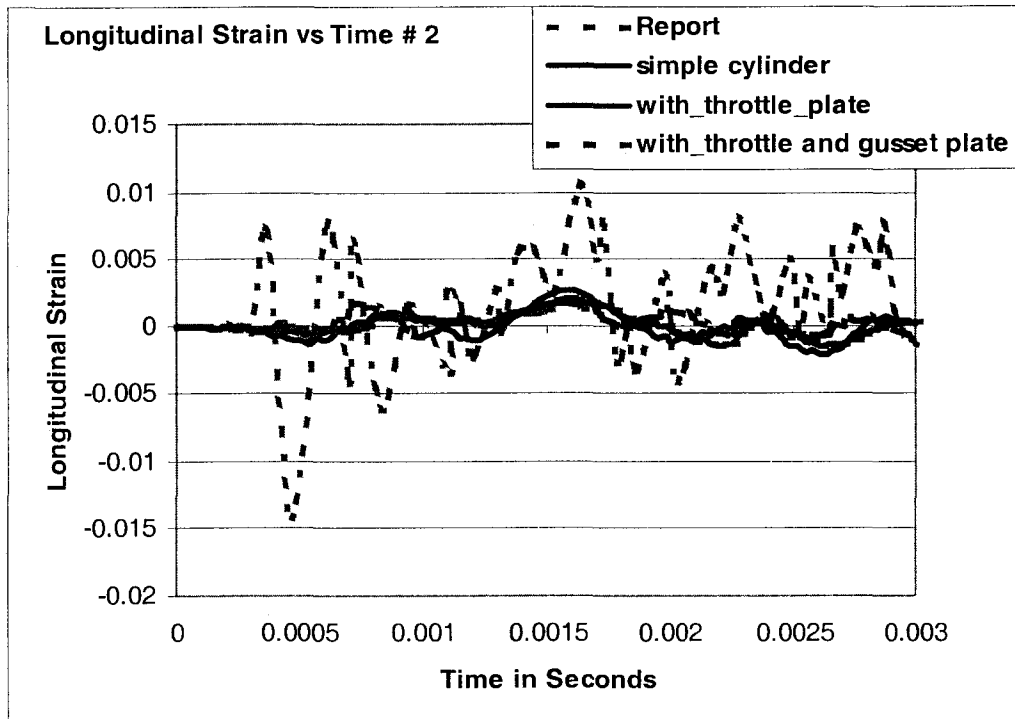


Figure 4.6 Longitudinal Plots for First Three Containers at # 2

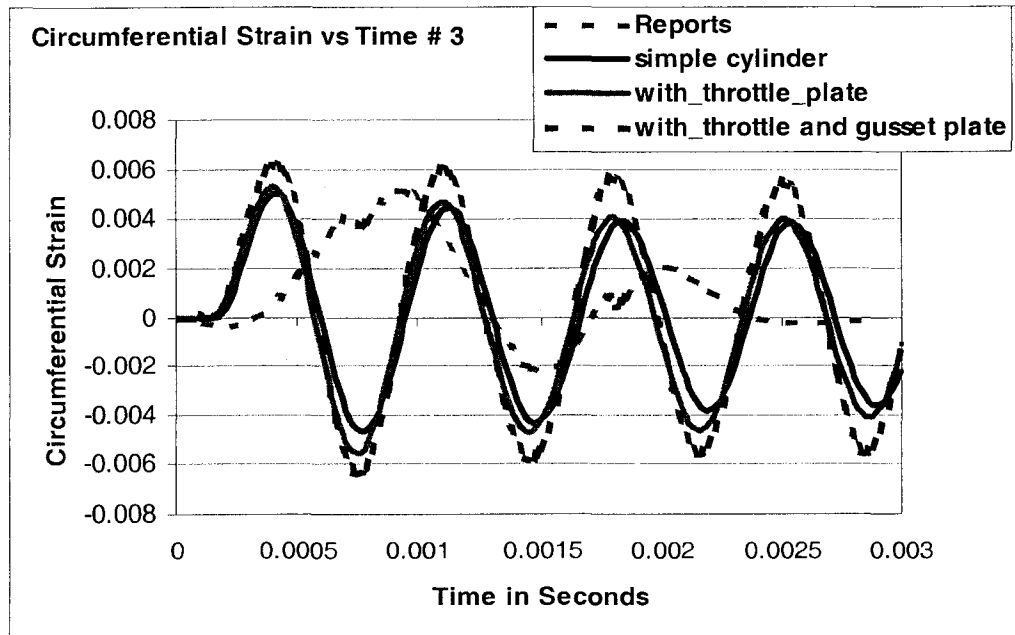


Figure 4.7 Circumferential Plots for First Three Containers at # 3

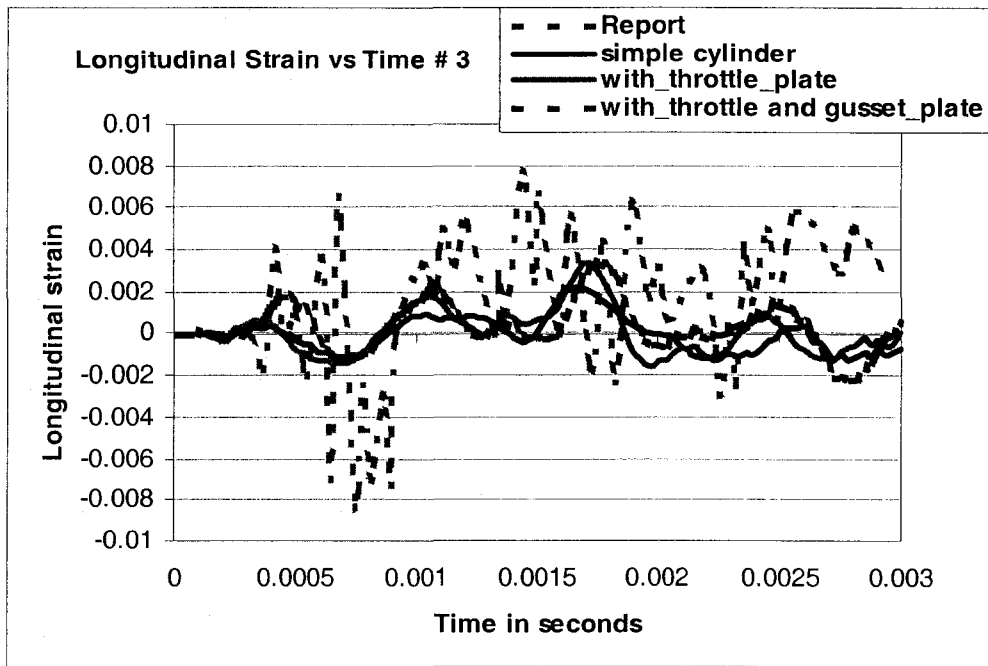


Figure 4.8 Longitudinal Plots for First Three Containers at # 3

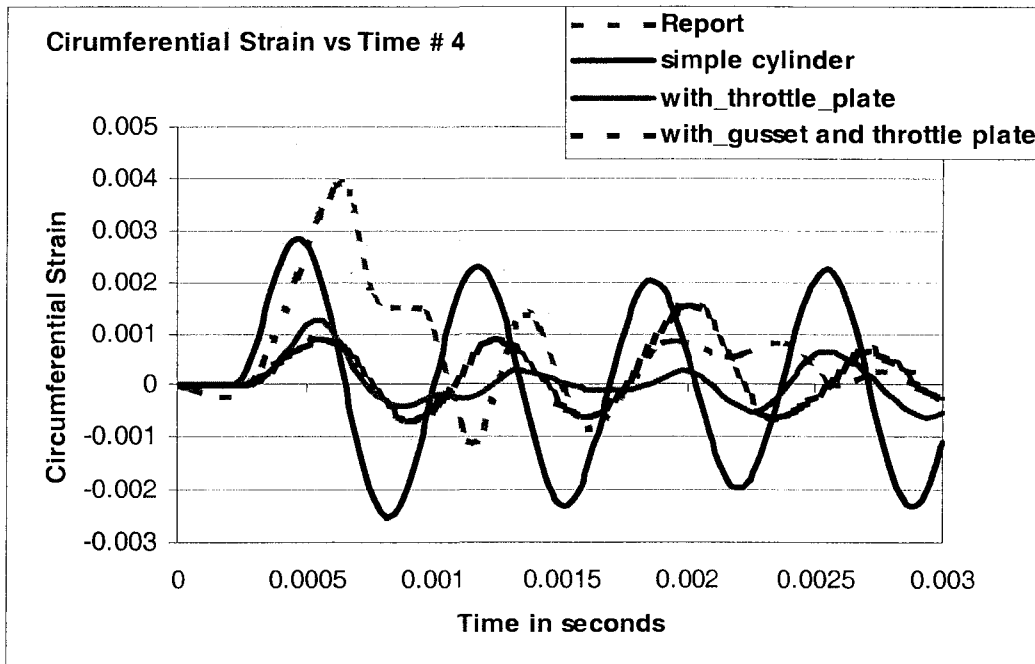


Figure 4.9 Circumferential Plots for First Three Containers at # 4

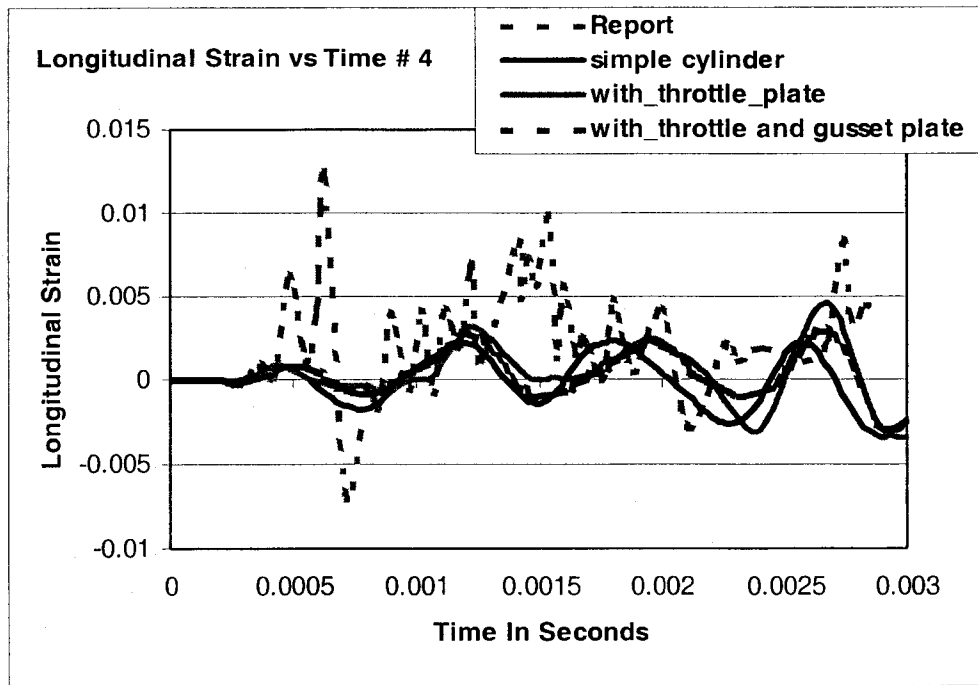


Figure 4.10 Longitudinal Plots for First Three Containers at # 4

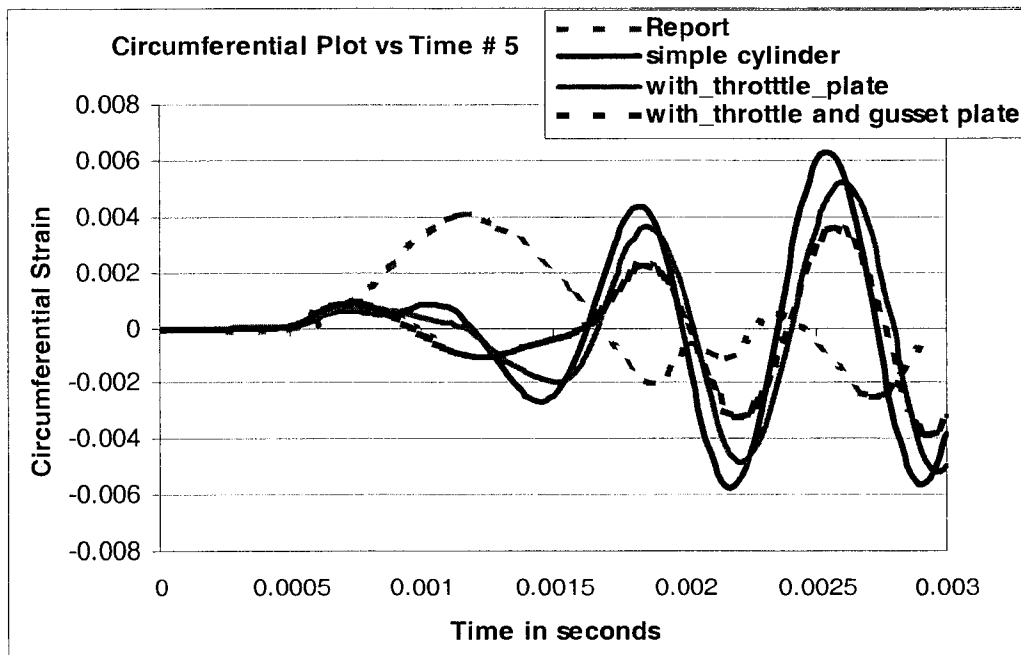


Figure 4.11 Circumferential Plots for First Three Containers at # 5

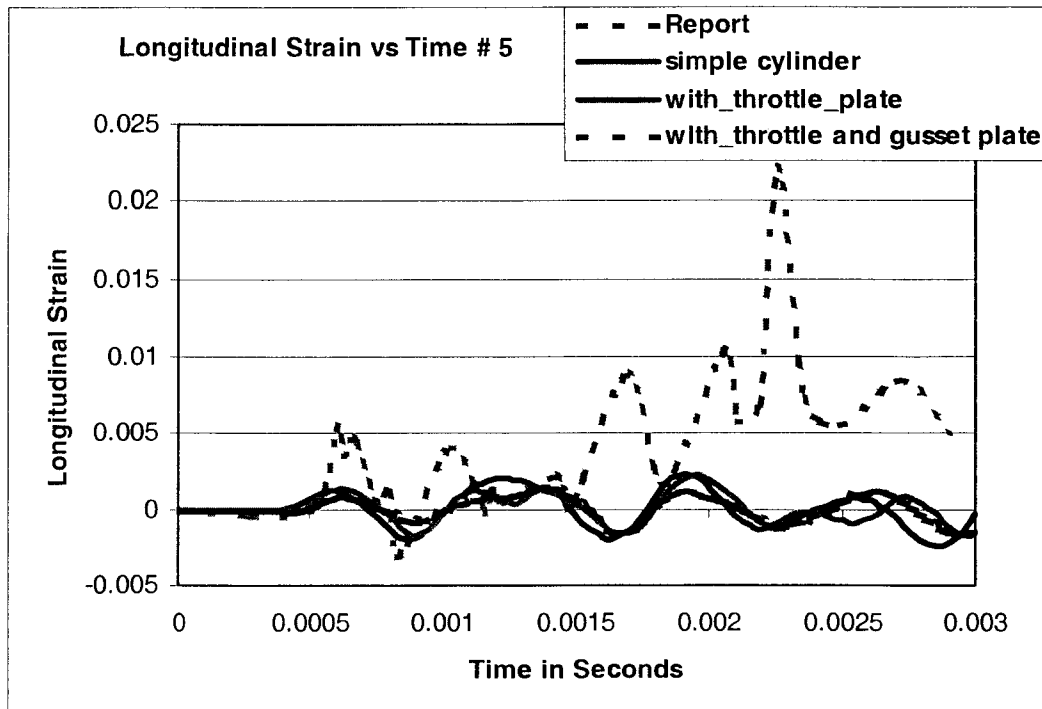


Figure 4.12 Longitudinal plots Plots for First Three Containers at # 5

4.2 Results and Discussion for Container # 2

The results for the second vessel model are as follows. Deformed Shapes, displacements and stresses were generated using LS-Post and Hyper-view. The following Figure 4.13 represents the Maximum circumferential stress has been observed as 899 mega pascal's at time equal to .14399 milli seconds. From the Figure 4.3, it is observed that the circumferential strains are less in magnitude and the material seems to be more elastic when compared to the results form the report [1]. Reduction in the magnitude when compared to the results [1] may be due to the replacement of different materials with a single shell. The magnitude of the circumferential strains at #1 and # 2 are observed to be same with and with out the throttle plate as the throttle plate is at the fourth point. From the longitudinal strain plot Figure 4.4, it is observed that the strain in

the longitudinal direction is smaller in magnitude when compared to the results from the report [1]. The chosen shell element is unable to capture the peak strains in the longitudinal direction. The frequency of the peaks and troughs are more in case of the results from the reports [1]. The peak circumferential strain value at the point 2 is greater in magnitude than the peak value when compared to the results from report [1], which is due to the more elastic nature of the shell element. The peak strain at this point is less than the previous point. The circumferential plots at the points 3 and 4 are reduced in magnitude when compared to the previous points but due to the elastic nature of the element the strains were more in case of the observed results from LSDYNA. The reduction in the elastic nature can be observed with the addition of the throttle plate. The circumferential plot at point 5 was quite different from the other plots and the reason may be due to the sudden reduction in the thickness. The reduction in the longitudinal strains at other points may be due to the material, which is unable to capture the strains in the longitudinal direction.

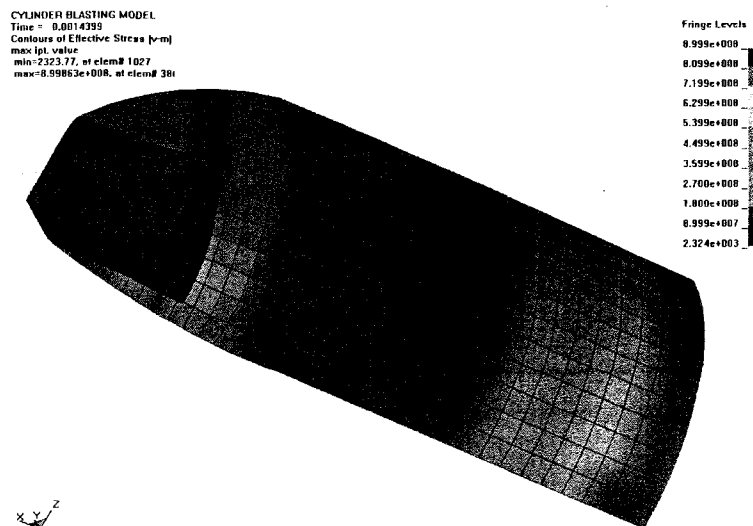


Figure 4.13 Maximum Circumferential Stress at Time t = .14399 milli sec

4.3 Results and Discussion for Container # 3

The following Figure 4.14 represents the Maximum circumferential stress has been observed as 962.9 mega pascal's at time equal to .1439 milli seconds. The magnitude of the circumferential strains at points #1 and # 2 are observed to be same in case of the first three models of the cylinders as the addition of the material is at the point 4. The reduction in the circumferential strain at the points # 4 and # 5 is due reduction in the flexibility of the shell by the addition of the material. From the longitudinal strain plot Figure 4.4, it is observed that the strain in the longitudinal direction is smaller in magnitude when compared to the results form the report [1]. The chosen shell element is unable to capture the peak strains in the longitudinal direction. The frequency of the peaks and valleys are more in case of the results from the reports [1]. The reduction in the longitudinal strains at other points may be due to the material, which is unable to capture the strains in the longitudinal direction.

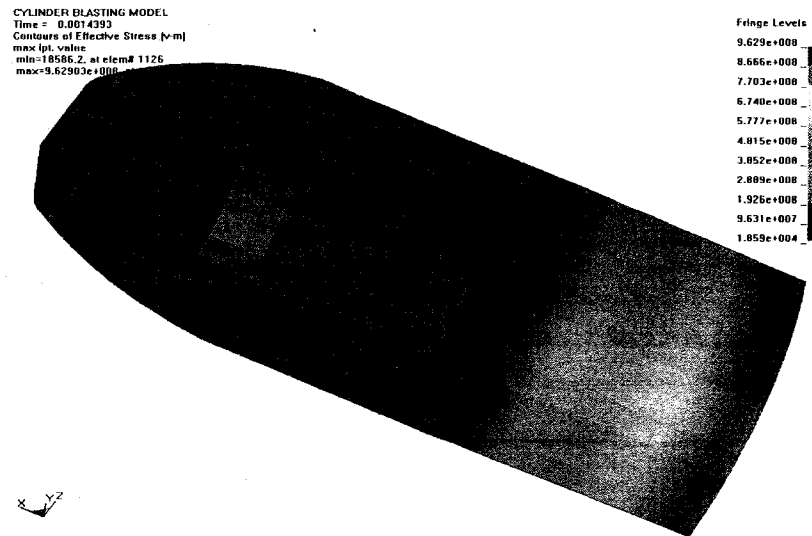


Figure 4.14 Maximum Circumferential Stress at Time $t = 0.1439$ milli sec

4.4 Results and Discussion for Container # 4

Following figure 4.15 represents the Maximum circumferential stress has been observed as 934.1 mega pascal's at time equal to 1.8 milli seconds. The strain histories have been plotted and compared to the sixth model results, which had simple foam and steel in the end portion. From the circumferential strain plot at point # 1 as shown in the Figure 4.15, it can be observed that the peak circumferential strain from the results from the reports [1] were in between the results from the two models. Solid elements are more reasonable in terms of frequency compared to shell elements. From the following longitudinal strain plot Figure 4.17, it can be observed that the strain in the longitudinal direction is smaller in magnitude when compared to the results form the report [1]. The frequency of the peaks and valleys are more in case of the results from the reports. Longitudinal strains for solids were more reasonable compared to shell elements but the values are insignificant when compared to the results [1]. The peak circumferential strain value at the point 2 and 3 was greater in magnitude than the peak value from the report [1] but results from the solid model were more reasonable when compared to shell elements. The circumferential plots at the points 4 are reduced in magnitude and have shown a phase shift and are more reasonable when compared to the shell element model. The circumferential plot at point 5 shows that the strains in the results were much greater than the strains from both the models. The reduction in the longitudinal strains may be due to the material, which is unable to capture the strains in the longitudinal direction.

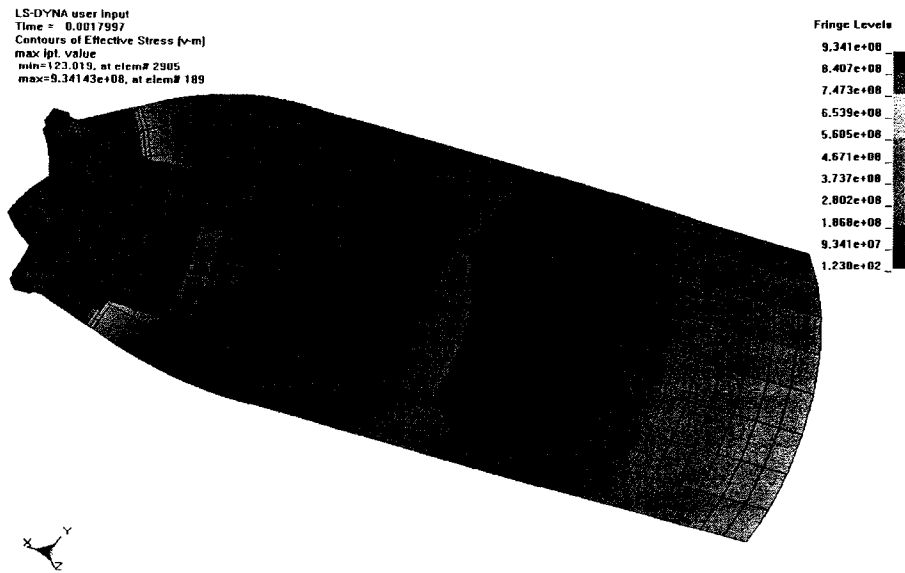


Figure 4.15 Maximum Circumferential Stress at Time $t = 1.8177$ milli sec

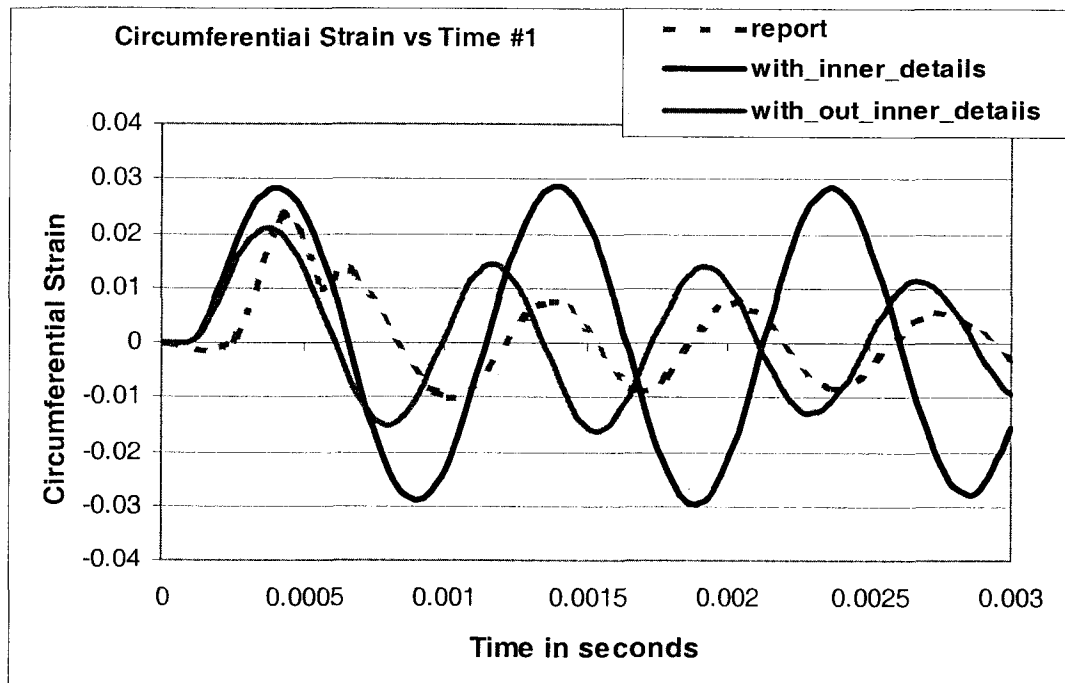


Figure 4.16 Circumferential Plots for the Fourth and Sixth Container at # 1

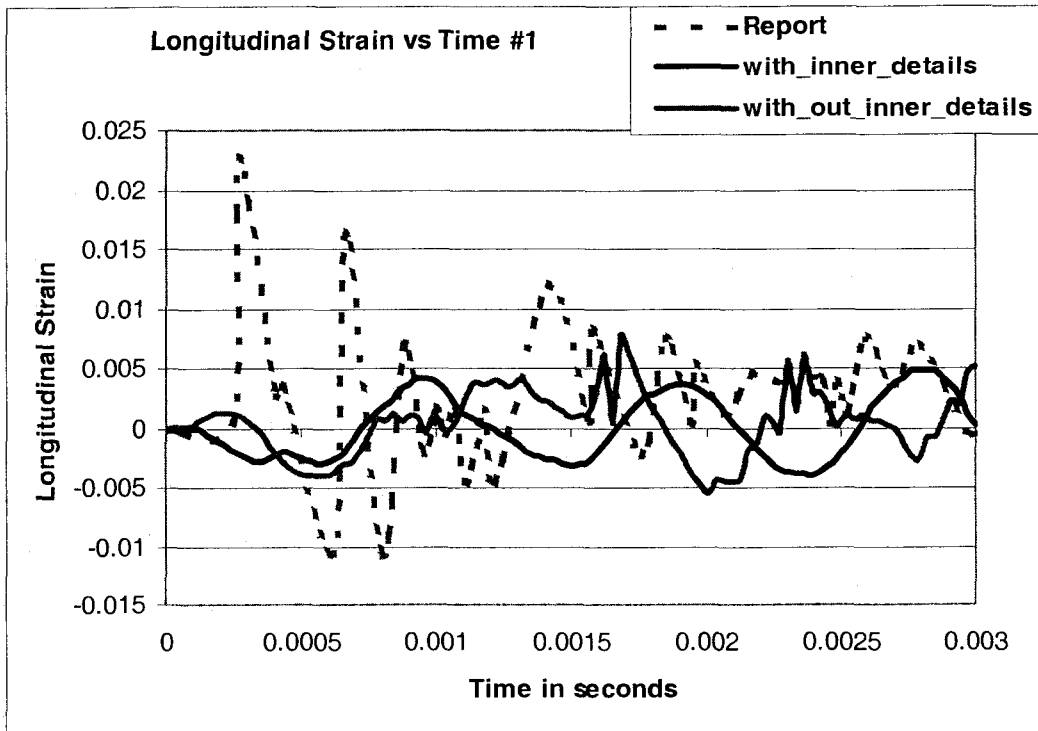


Figure 4.17 Longitudinal Plots for the Fourth and Sixth Container at # 1

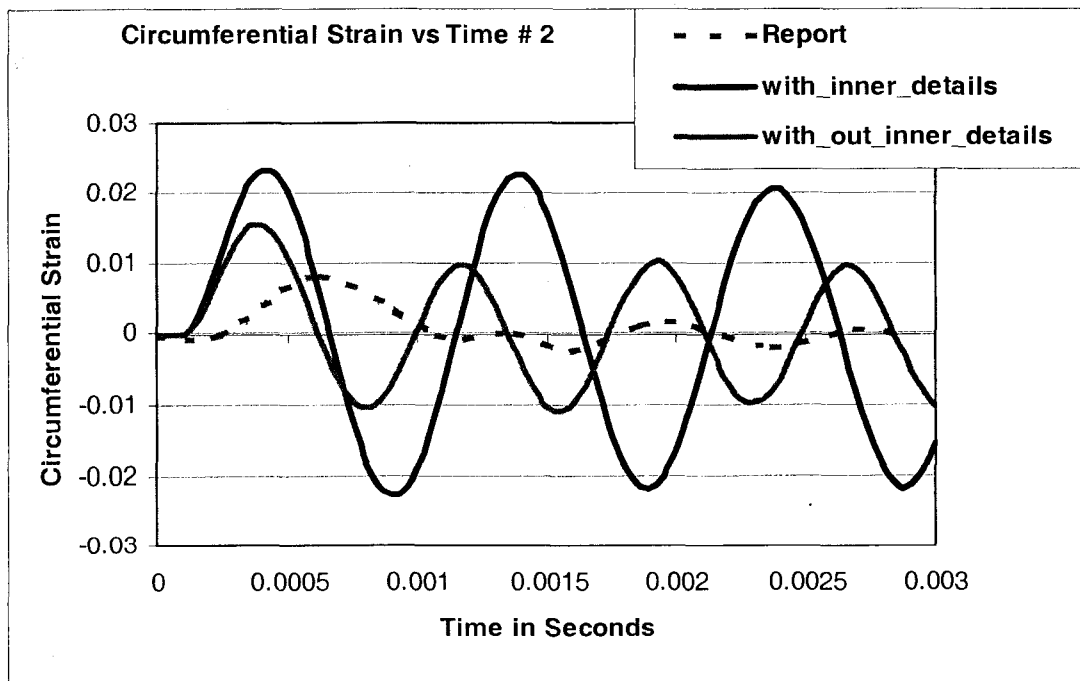


Figure 4.18 Circumferential Plots for the Fourth and Sixth Container at # 2

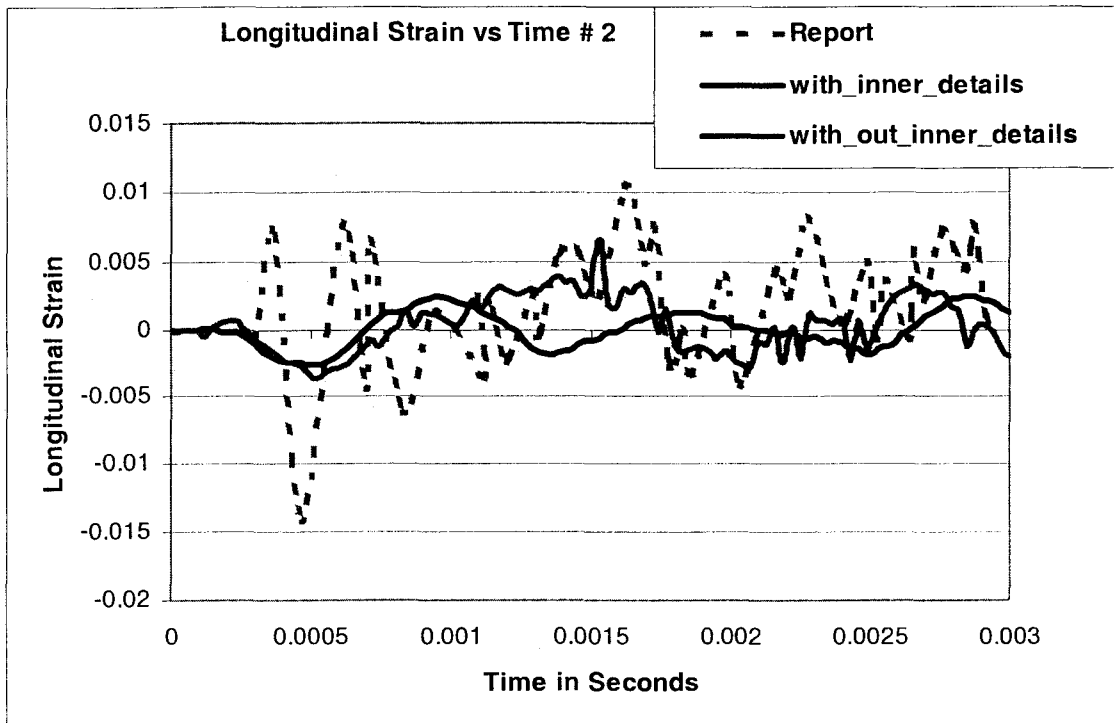


Figure 4.19 Longitudinal Plots for the Fourth and Sixth Container at # 2

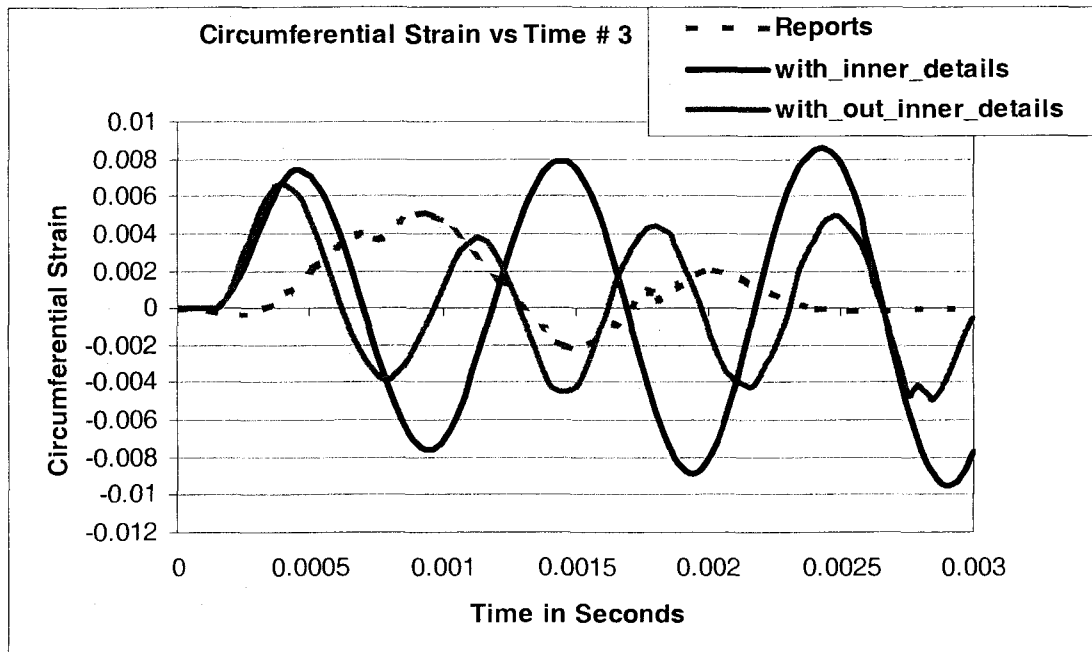


Figure 4.20 Circumferential Plots for the Fourth and Sixth Container at # 3

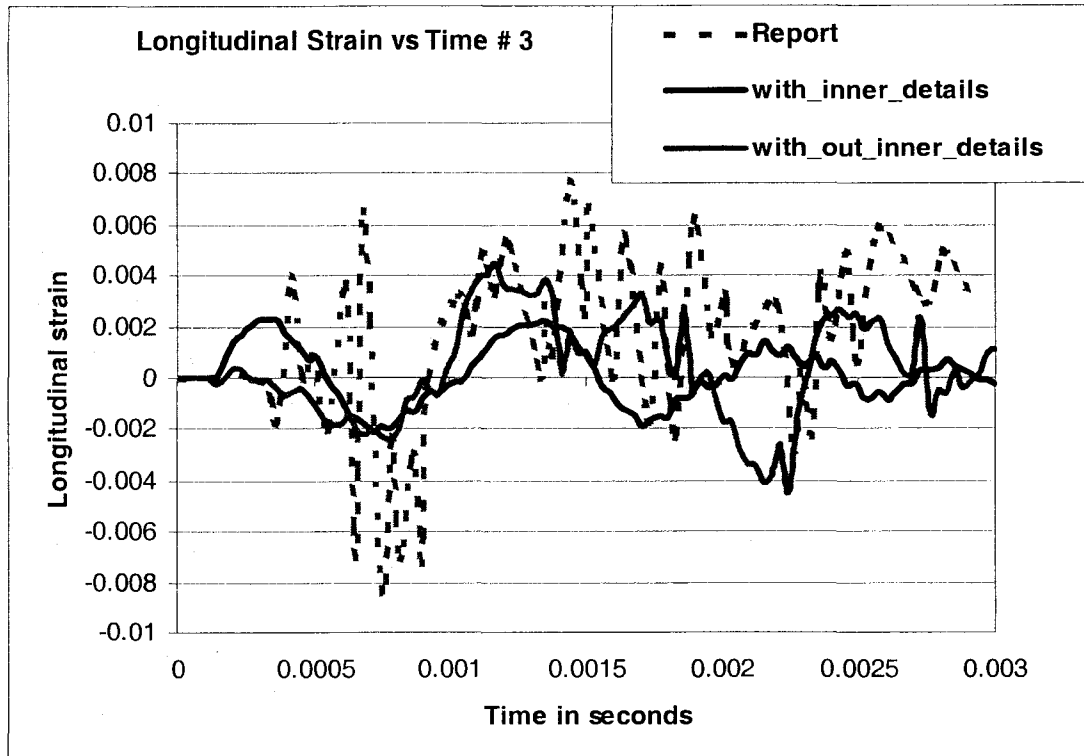


Figure 4.21 Longitudinal Plots for the Fourth and Sixth Container at # 3

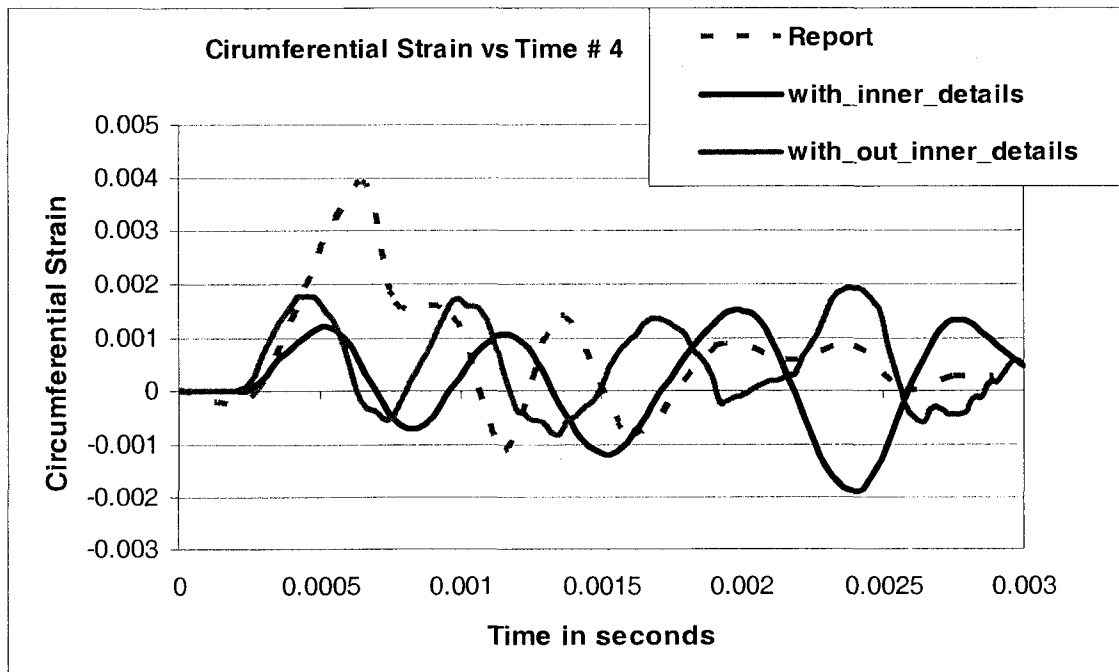


Figure 4.22 Circumferential Plots for the Fourth and Sixth Container at # 4

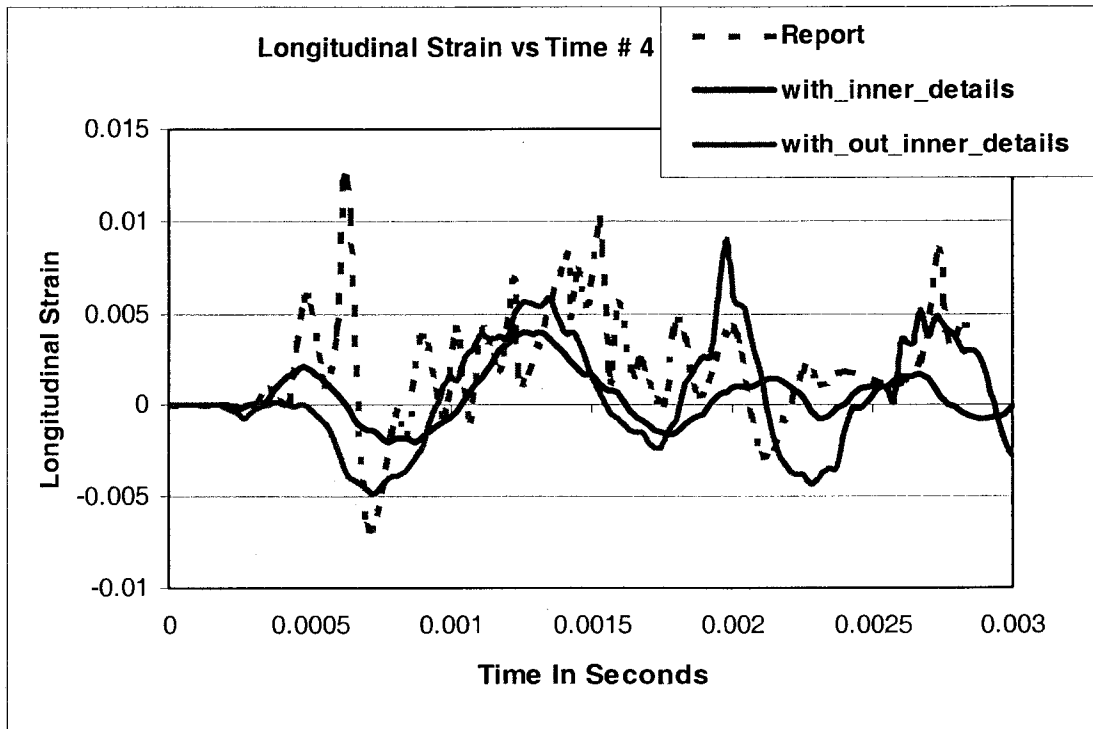


Figure 4.23 Longitudinal Plots for the Fourth and Sixth Container at # 4

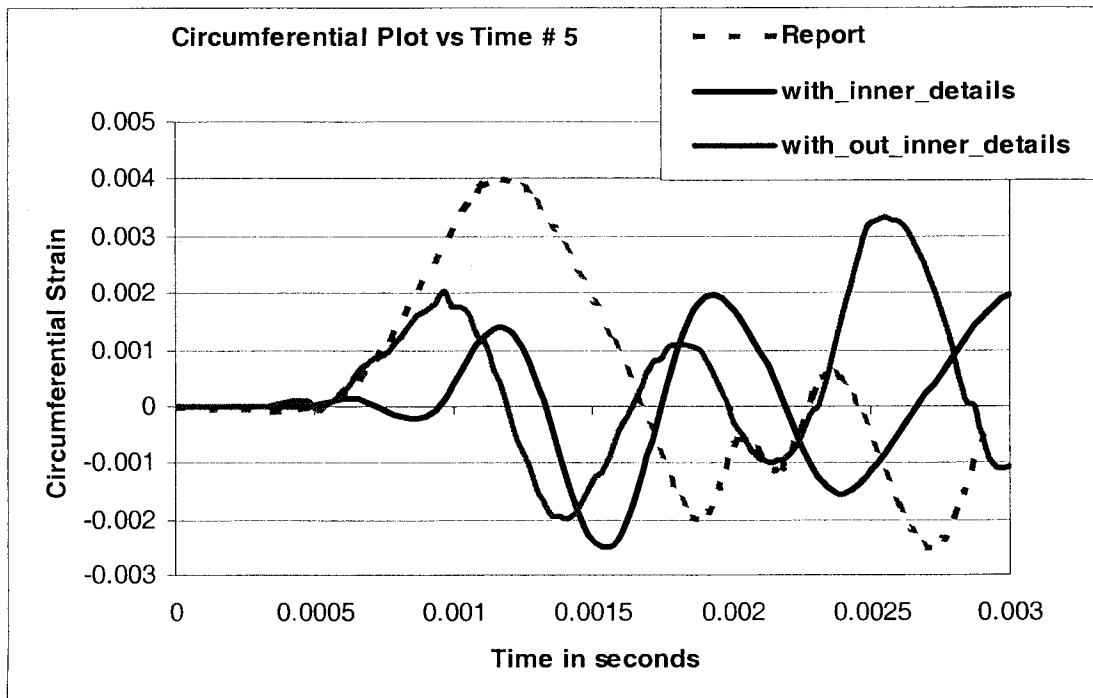


Figure 4.24 Circumferential Plots for the Fourth and Sixth Container at # 5

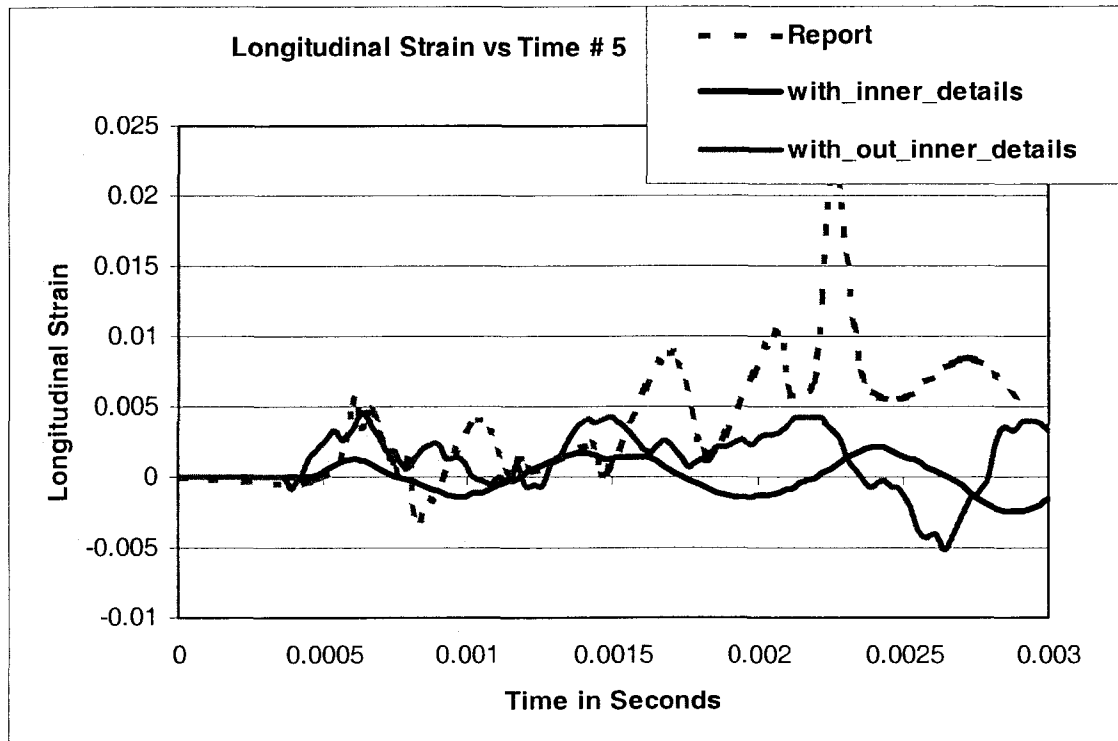


Figure 4.25 Longitudinal Plots for the Fourth and Sixth Container at # 5

4.5 Results and Discussion for Containers # 5 and # 6

The results for the fifth and sixth vessel models are as follows. Deformed Shapes, displacements and stresses have been generated using LS-Post and Hyper-view. The following Figures 4.26 and 4.27 represents the Maximum circumferential stresses. The strain histories have been plotted and compared to the two dimensional model results from the reports. A maximum circumferential stress for the vessel model 5 was $1.222e9$ Pa at time $t=3.9$ milli sec. Maximum circumferential stresses for the vessel model 6 was $1.357e9$ Pa at time $t=.79$ milli sec. The circumferential strains were less in magnitude when compared with the results from the reports [1]. The magnitudes of the stresses were more compared to the shell models and the solid elements are less elastic as the gradual decrease in the amplitude is observed with time. The circumferential strains at all the

points for both the solid models were almost the same. The addition of the gusset plate has not changed the magnitude of the circumferential stresses to a greater magnitude. The magnitude of the longitudinal strains at all the points was significantly low when compared to the results from the reports [1]. The frequency of peaks and valleys were much better when compared to the strains from the shell models. Although solid models have better strains they are unable to get the data of all the peaks and valleys.

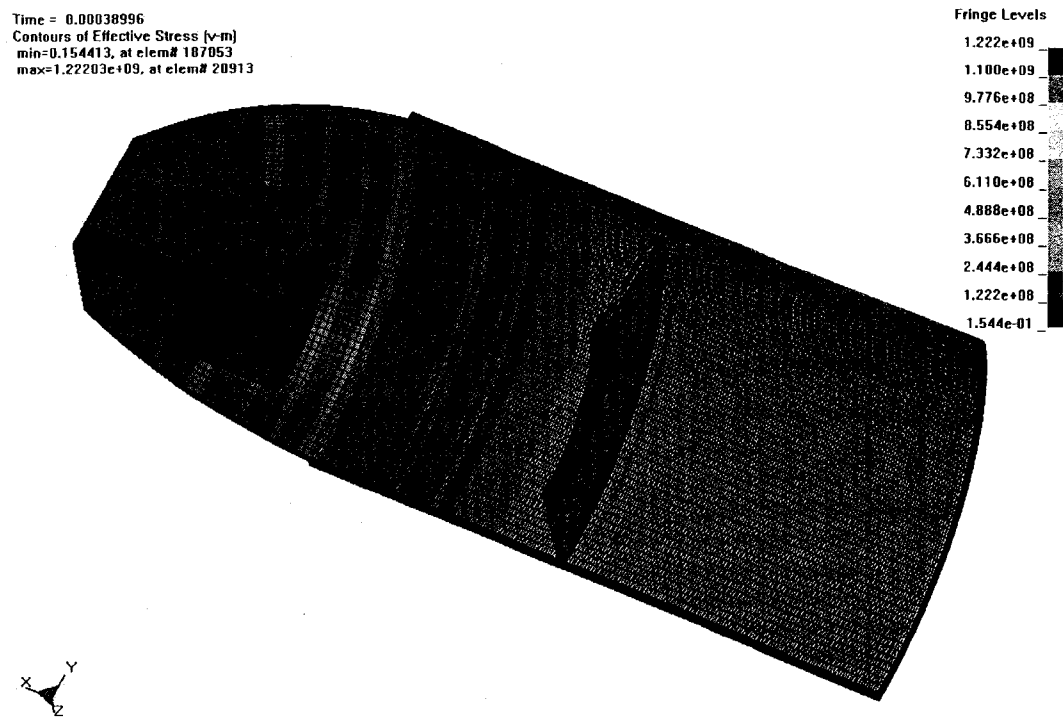


Figure 4.26 Maximum Circumferential Stresses at Time $t = 3.9$ milli sec

Time = 0.00077993
 Contours of Effective Stress (v-m)
 min=230.325, at elem# 236925
 max=1.31742e+09, at elem# 329050

Fringe Levels
 1.317e+09
 1.186e+09
 1.054e+09
 9.222e+08
 7.905e+08
 6.587e+08
 5.270e+08
 3.952e+08
 2.635e+08
 1.317e+08
 2.303e+02

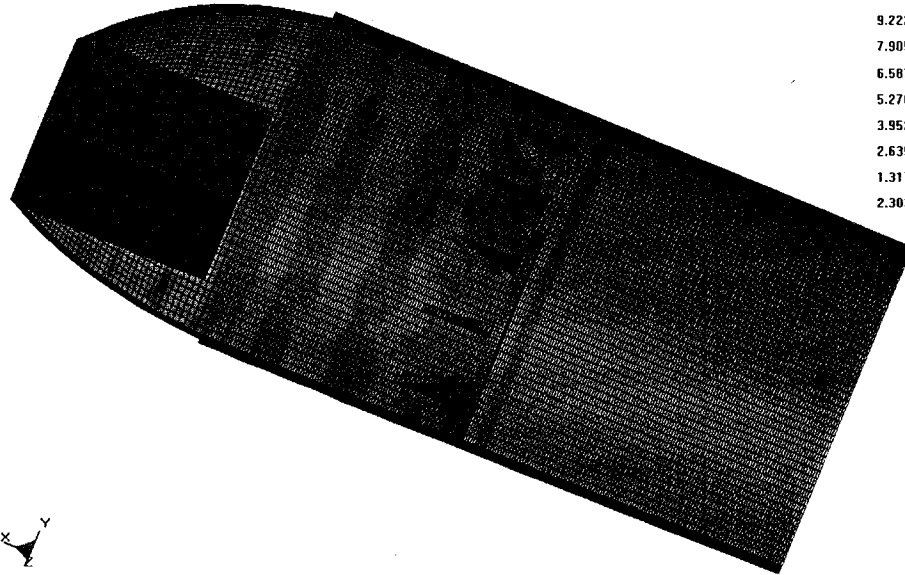


Figure 4.27 Maximum Circumferential Stresses at Time t = .799 sec

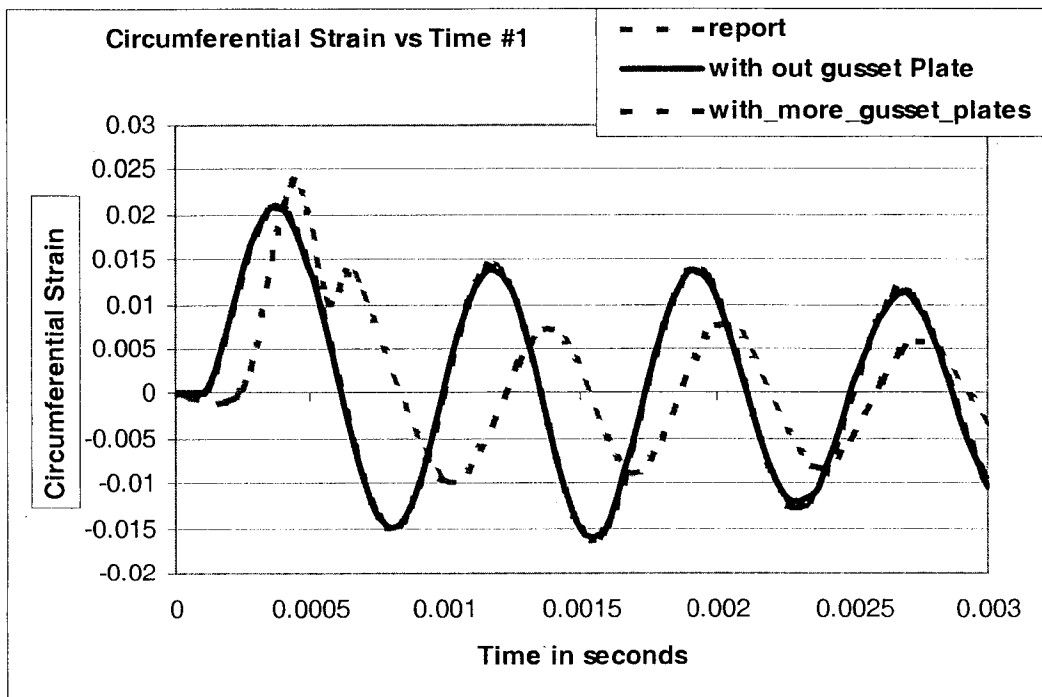


Figure 4.28 Circumferential Plots for Five and Six Containers at # 1

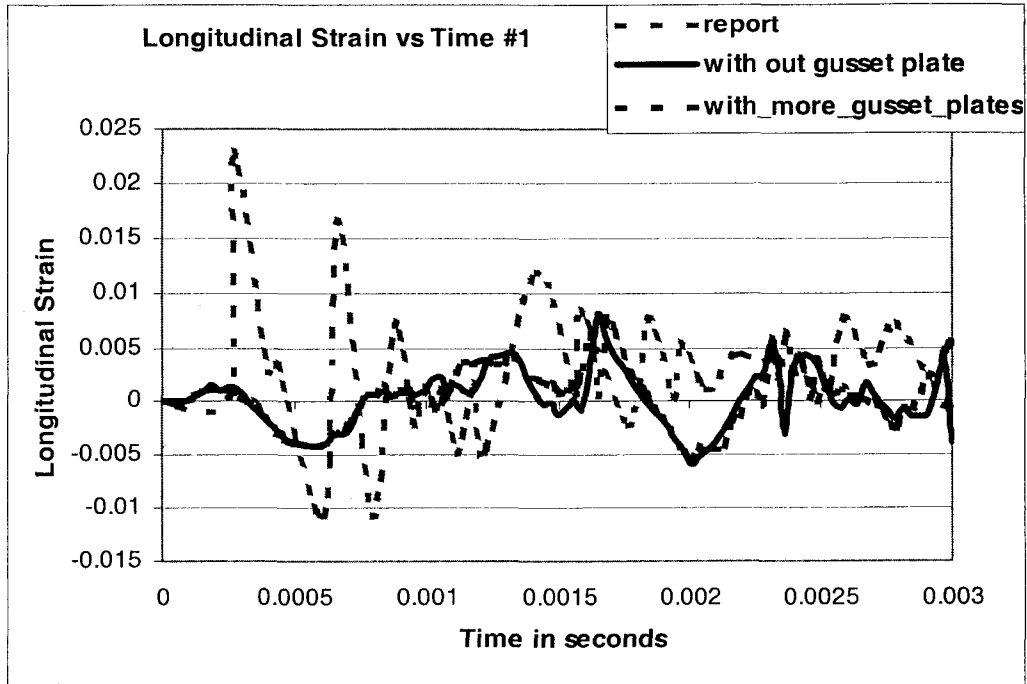


Figure 4.29 Longitudinal Plots for Five and Six Containers at # 1

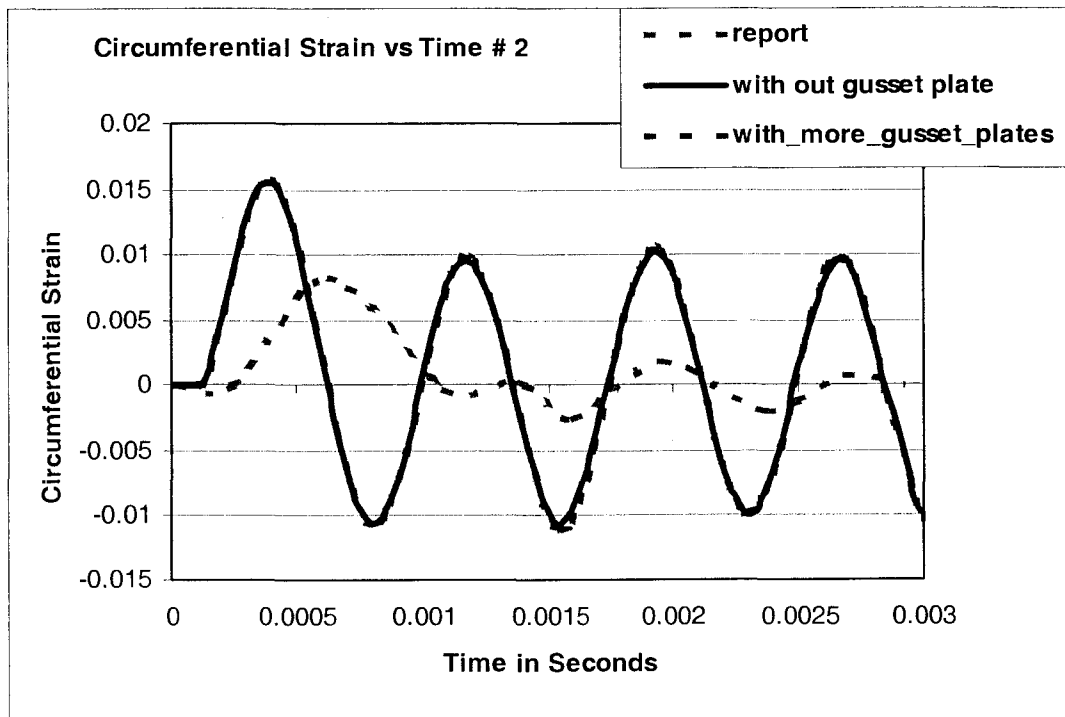


Figure 4.30 Circumferential Plots for Five and Six Containers at # 2

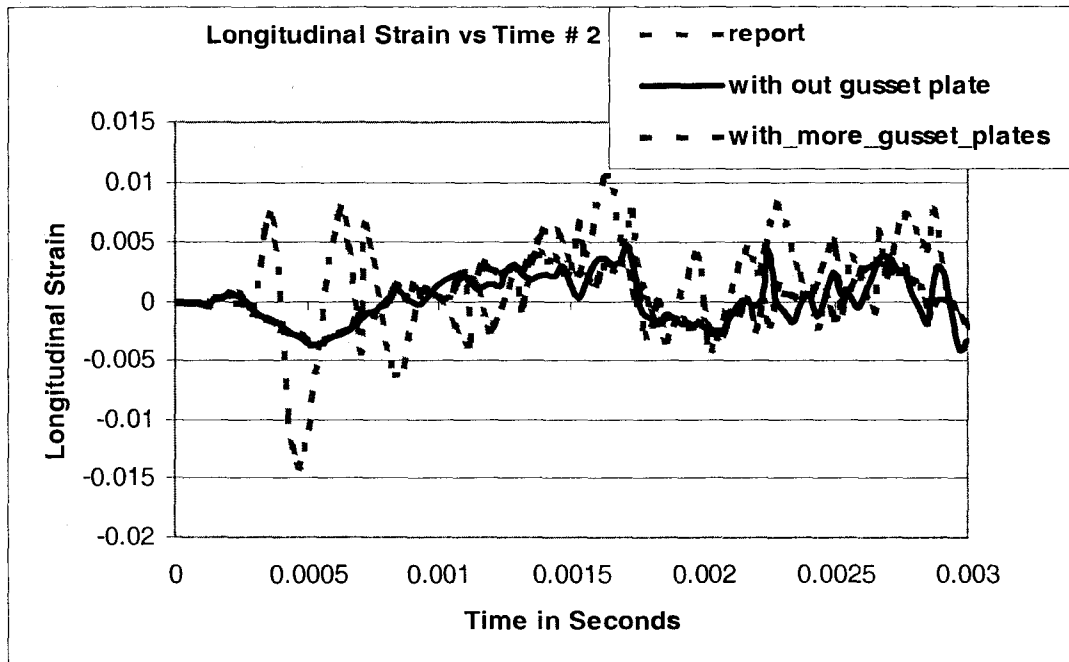


Figure 4.31 Longitudinal Plots for Five and Six Containers at # 2

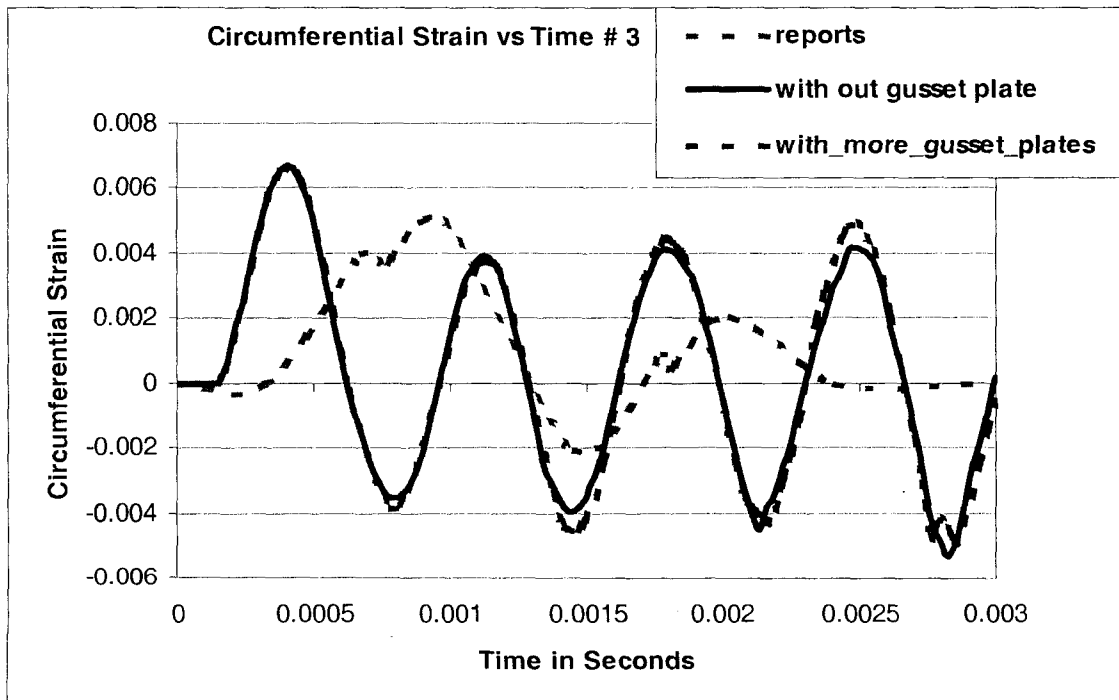


Figure 4.32 Circumferential Plots for Five and Six Containers at # 3

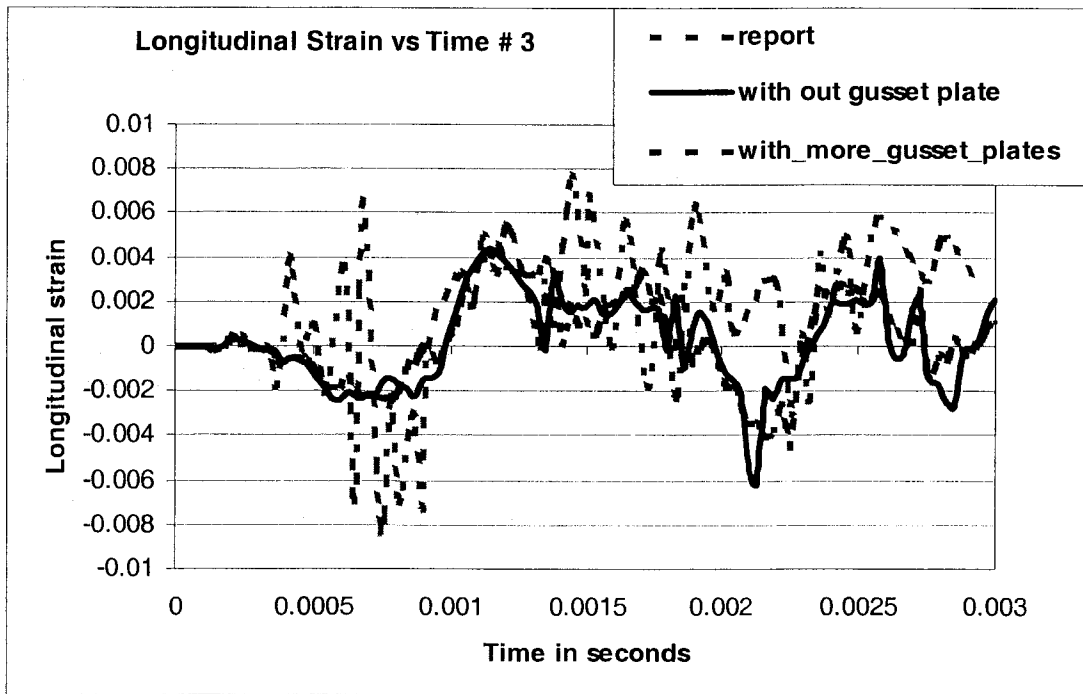


Figure 4.33 Longitudinal Plots for Five and Six Containers at # 3

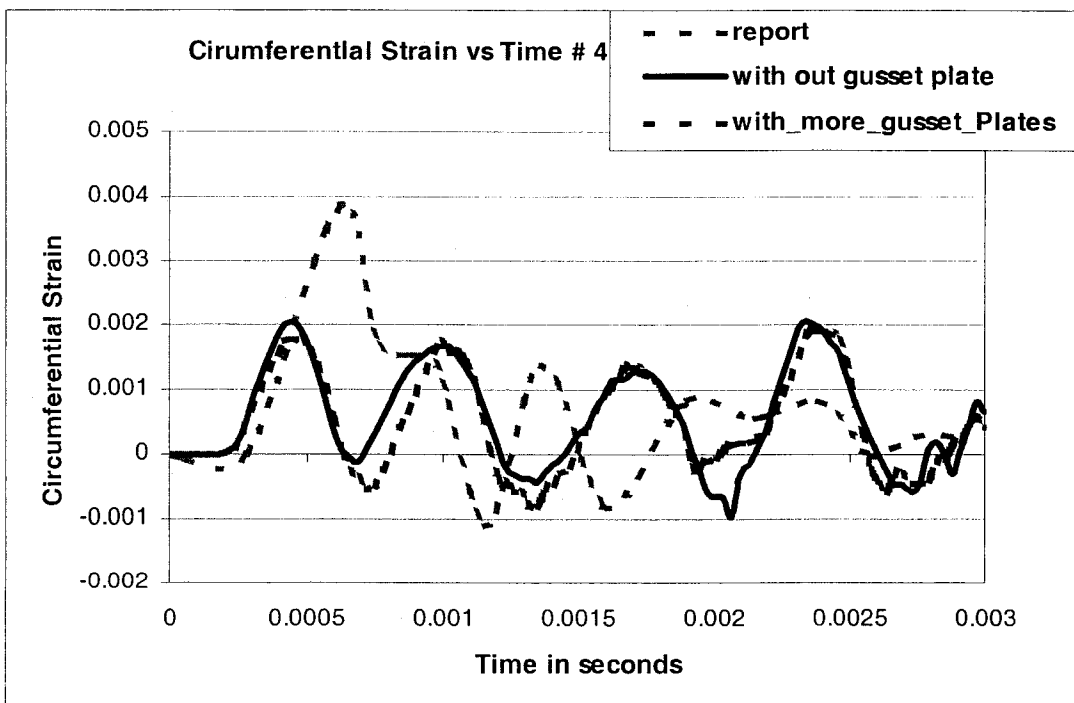


Figure 4.34 Circumferential Plots for Five and Six Containers at # 4

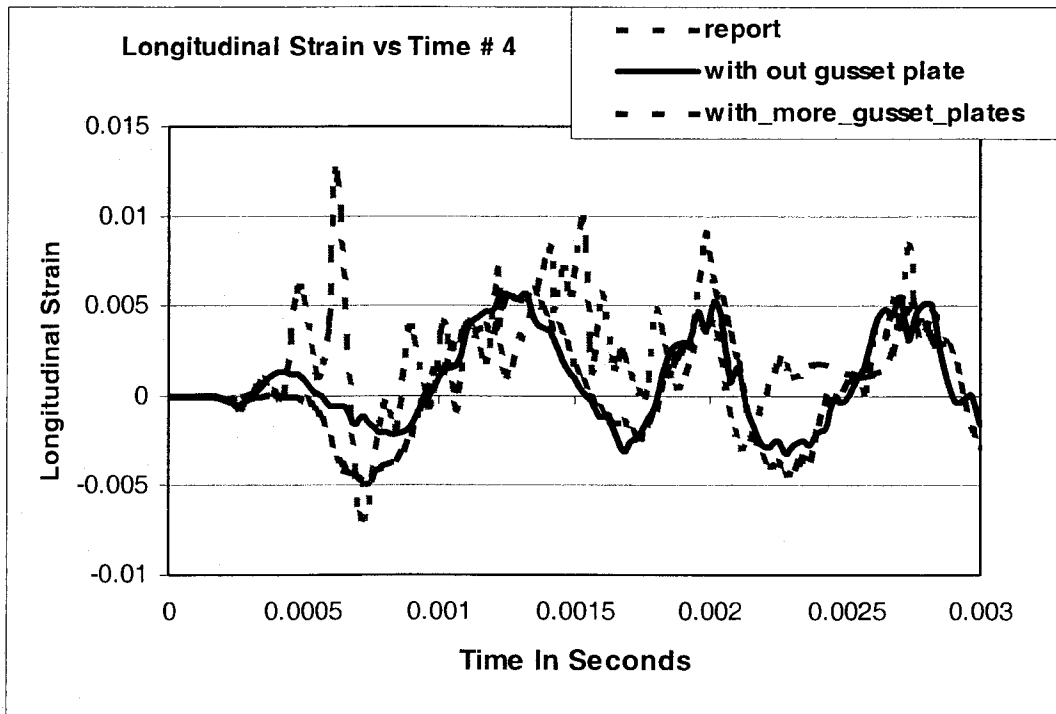


Figure 4.35 Longitudinal Plots for Five and Six Containers at # 4

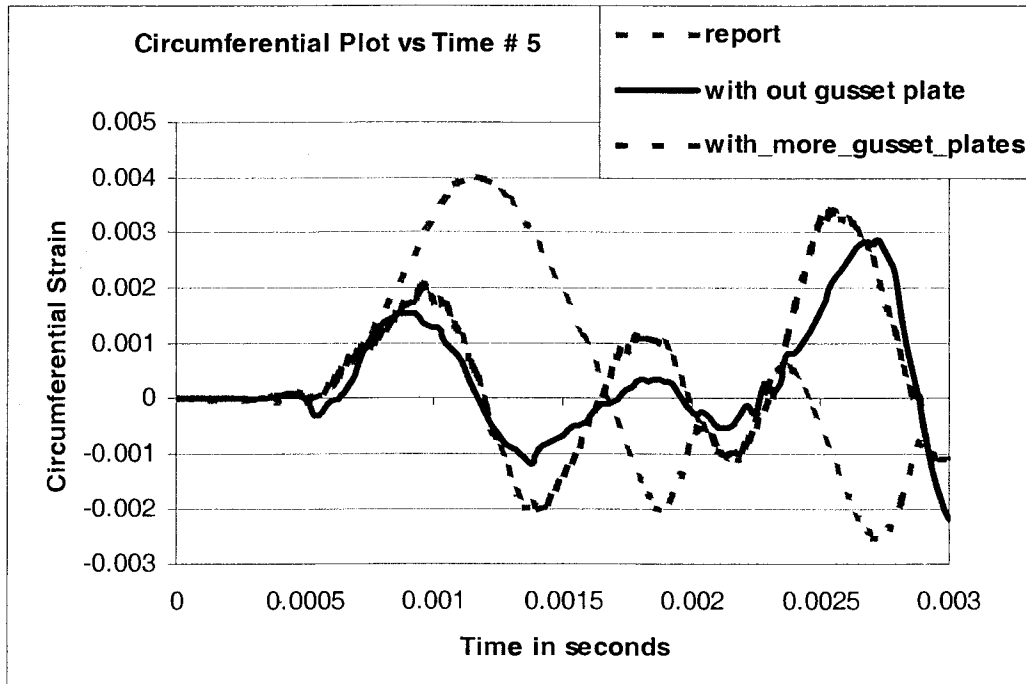


Figure 4.36 Circumferential Plots for Five and Six Containers at # 5

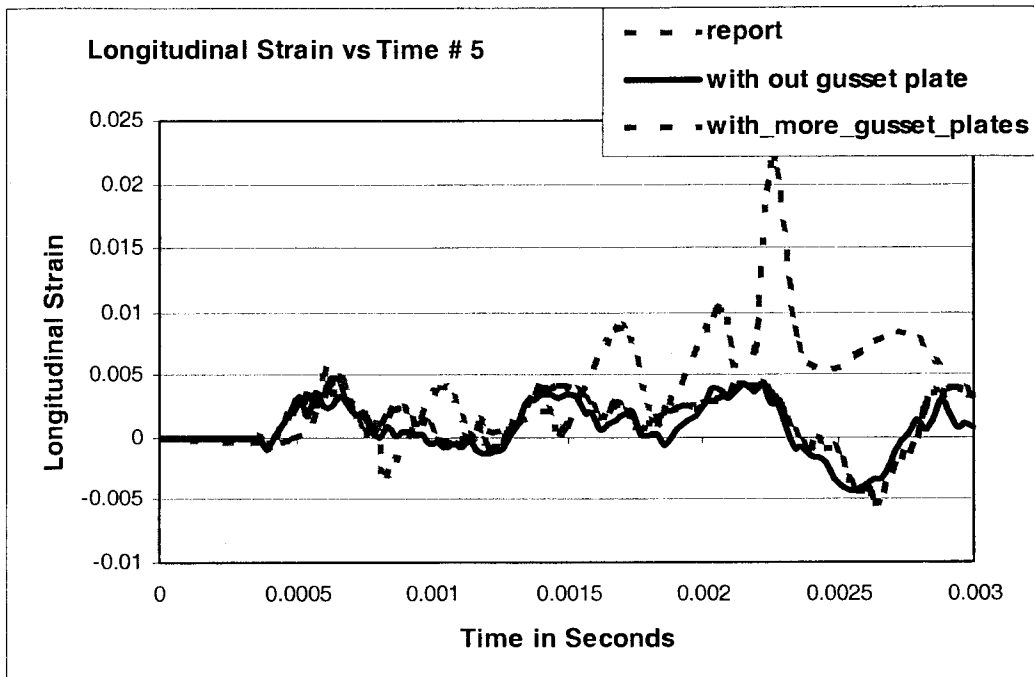


Figure 4.37 Longitudinal Plots for Five and Six Containers at # 5

CHAPTER 5

CONCLUSIONS

5.1 Conclusions:

This research was focused on the modeling of the full containment vessel by gradually moving toward the more realistic model of the vessel and to determine the effectiveness using the material models with in LS-DYNA. This research also focuses on the prediction of the maximum deformations in the composite or steel structure.

The strains from the LS-DYNA were more reasonable when compared to the strains from the 2-D simulations. In the results from 2-D simulations the magnitude of the peak strains in circumferential and longitudinal directions were almost the same. In general the circumferential strain is equal to the twice the axial strain. The results from LS-DYNA were more reasonable with respect to the circumferential and axial strains. Results from the solid elements were more reasonable compared to the results from the shell elements. Shell elements are more elastic in nature compared to solid models. Solid models were able to predict the strains to a greater extent compared to shell models. Addition of the gusset plate in the models has not changed the strains to a greater magnitude. The accuracy in the results from LS DYNA using CONWEP in this case was less reliable and inversely proportional with respect to distance from the point of explosion.

5.2 Future Goals Involved in this Project are as Follows

- To conduct computational simulations using LSDYNA of the open cylinder experiments conducted by the Russian Federal Nuclear Center (RFNC-VIIEF).
- Increase the number of elements through the thickness of the cylindrical portion of the model.
- Including the damping effects, EOS for material models, Steel mesh for anti-fragment materials.
- ALE analysis of the open containers.
- To Conduct the ALE simulation of the complete closed cylinder.
- Compare the results between the CONWEP and ALE.
- Conduct the parametric studies to investigate the effect of several design vessel variables on vessel performance.
- Investigating the various optimization parameters such as:
 1. Composite material failure modes with in the analysis code.
 2. Throttle plate to steel containment attachment conditions.
 3. Gusset Plate Size and attachment conditions.
 4. Interface properties between steel and composite materials.
 5. Effect of foam on the door loading.
 6. Stress concentrations around the cutout parts.

REFERENCES

- [1] Explosion-Proof Container, Theoretical and Computational studies under the contract # AX-3828 between Sandia Corporation (USA) and RFNC-VNIIEF.
- [2] Evaluation of damage and TNT equivalence of ammunition, explosive and pyrotechnics by Pushpa Buri, MM Verma, and Harbans Lal.
- [3] Rogers, G.L., Dynamics of Structures, John Wiley, New York, 1959
- [4] Dharaneepathy, MV Rao, MNK and Santhakumar A.R Critical distance for blast resistant design, Comp & Struct v 52 No 4 Feb 17 1994 Pergamon Press Inc
- [5] Ayvazyan,H.,Dobbs,Dede N .,Whitney,M., Bowles,P., Baker,W and Caltagirone, J.P Structures to resist effects of accidental explosions ,baker W.E.,V II, Blast Fragments and Shock Loads, Special Publication no AD-A 673 U.S Army Armament Research Development and Engineering Center ,Dover NJ,1983.
- [6] Transient Response of Laminated Plates Subjected to Close proximity Explosions, John M Coggin, Jeffrey M.K.Chock, Rakesh K Kapania, Eric R.Johnson.
- [7] A representative survey of blast loading models and damages assessment methods for buildings subjected to Explosive Blasts.
- [8] Dynamic Behavior of Concrete Structures subjected to Blast and Fragment Impacts, JOOSEF LEPPÄNEN, Department of Structural Engineering, Concrete Structures, CHALMERS UNIVERSITY OF TECHNOLOGY, Göteborg, Sweden 2002.
- [9] LS-Dyna Theory Manual and LS DYNA version 970, keyword user manual.

- [10] <http://erl.org/docs/facility%20protection/01%20%20blast,%20chemical,%20biological%20and%20other%20force%20protection%20threats/04%20Blast%20effect-related%20threats.pdf>
- [11] Material for the Input deck cards has been taken from LS DYNA-960 volume 1
- [12] Explosive blast, fema 426_ch4.pdf, Premier for design of commercial buildings to mitigate the Terrorist Attacks, pages 4-1 to 4-20.
- [13] E.J.Barbero, Introduction to Composite Materials Design, Taylor & Francis, 1999.
- [14] LS DYNA –Theory manual
- [15] Explosive shocks in Air by Gilbert F Kinney and Kenneth J Graham, page 90-95.
- [16] TM 5-855-1 (Department of the Army 1986)
- [17] TM 5-1300 of U.S. Departments of the Army, Navy, and Air Force 1990.
- [18] Johansson and Persson 1970, Baker 1973, Baker et al. 1983

VITA

Graduate College
University of Nevada, Las Vegas

Local Address:

4217 Cottage Circle # 3,
Las Vegas, Nevada, USA- 89119

Home Address:

49-38-20/1, Akkayapalem,
N.G.G.O'S Colony,
Visakhapatnam, Andhra Pradesh,
India -530016

Degrees:

Bachelor of Technology, Mechanical Engineering, 2001
Jawaharlal Nehru Technological University, India.

Thesis Title: Computational Simulation of Internal Blast Loading on Containment Vessels

Thesis Examination Committee:

Chairperson, Dr. Mohamed Trabia , Ph. D.
Chairperson, Dr. Brendan J.O'Toole , Ph. D.
Committee Member, Dr. Ajit .K.Roy, Ph. D.
Committee Member, Dr. John Wang, Ph. D.
Graduate College Faculty Representative, Dr. Samaan Ladkany, Ph. D.